

# Indentation-Based Material Parameter Identifiability in Anisotropic Soft Tissues

Amit Ashkenazi<sup>a</sup>, Adi Shultz<sup>a</sup>, Lee Jordan<sup>a</sup>, Dana Solav<sup>a</sup>

<sup>a</sup>Faculty of Mechanical Engineering, Technion Institute of Technology, Haifa, Israel

---

## Abstract

Accurate quantification of soft tissue material parameters is essential for tissue mechanics simulations, medical device design, surgical planning, and non-invasive diagnostics. Finite element analysis (FEA) is commonly employed, but generating accurate simulations often requires patient- and location-specific tissue material parameters. Although soft tissue constitutive models are well-developed, practical implementation is limited by the invasive nature of experiments required for fitting model parameters. Non-invasive methods, such as indentation and suction, offer in vivo applicability but typically lack analytical solutions that would allow direct fitting of material parameters. Consequently, parameter identification becomes an inverse problem solved via FEA, which is often ill-posed, yielding multiple sets of seemingly optimal parameters, especially with limited experimental data. This non-uniqueness undermines the reliable prediction of tissue response under varying loads. This study investigates the identifiability of transversely isotropic hyperelastic material parameters through macro-scale indentation, combining simultaneous measurements of force and full-field surface deformation. We use a simplified two-parameter constitutive model to represent a soft composite phantom and compare the homogenized parameters identified through indentation with those obtained from separate analyses of the matrix and fiber materials. Our findings indicate that a measurement error of 5% leads to certainty bounds of  $\pm 5.2\%$  and  $\pm 28\%$  for the isotropic and anisotropic parameters, respectively, when utilizing combined force-deformation data. In contrast, when only force data is considered, they are  $\pm 22.5\%$  and  $\pm 210\%$ , respectively. These results demonstrate that surface deformation measurements are crucial for uniquely identifying anisotropic hyperelastic parameters through indentation. Further research is needed to evaluate identifiability in more complex models and in vivo indentation scenarios.

**Keywords:** Digital image correlation (DIC), Fiber-reinforced silicone phantom, Hyperelasticity, Inverse finite element analysis (iFEA), Optimization

---

## 1. Introduction

Accurate modeling and quantification of the mechanical responses of biological soft tissues are critical in various applications, including the design of medical devices that mechanically interact with tissues [1, 2, 3, 4, 5], the development of realistic tissue phantoms for surgical training [6, 7, 8], the construction of numerical simulations for surgical planning [9, 10, 11], and the development of diagnostic and prediction tools [12, 13, 14].

A key characteristic of many soft tissues is the presence of collagen fibers, which are significantly stiffer than the surrounding elastin [15]. Collagen fiber distribution results in highly nonlinear behavior and a pronounced anisotropy [16]. Moreover, the mechanical properties of these tissues are highly specific to both the anatomical region and the individual, with estimates differing by up to four orders of magnitude across and among individuals [17, 18]. Consequently, many applications necessitate mechanical properties assessment on a per-case and per-patient basis.

Although the mathematical formulations of the constitutive laws that describe the mechanical response of soft tissues are well-researched, much of the experimental work aimed at fitting the material parameters of these constitutive models relies on testing procedures that require invasive test specimen preparation. These procedures often disrupt and damage the tissues [19], making them unsuitable for in vivo applications.

To address this challenge, indentation (e.g., [20, 21, 22]) and suction (e.g., [23, 24, 25]) techniques have emerged as promising methods for non-invasive, in situ, or in vivo assessment of soft tissue material properties. Due to the lack of closed-form solutions for the stress-stretch relations in the general case of large-deformation indentations, parameter identification is performed using numerical inverse methods. These methods rely on finite element (FE)

simulations, in an approach that is typically referred to as inverse finite element analysis (iFEA) or finite element model updating (FEMU) [26, 27, 28]. This method involves iteratively adjusting the values of the material parameters to minimize the differences between simulation results and experimental measurements. Importantly, this process can be sensitive to the choice of experimental design and measurement modalities.

The task of identifying material parameters through iFEA involves several complexities and challenges. Even with standardized protocols, such as uniaxial and biaxial tension tests, material parameter identification can be challenging due to the occurrence of multiple sets of parameters that exhibit equivalent optimality [29, 30]. This non-uniqueness problem is amplified for large-deformation indentations [31, 32, 33, 34], especially when considering anisotropy [35, 36].

It is important to note that using any arbitrary set of parameters from these multiple options may not significantly affect results if the material is evaluated under loading conditions similar to those used during characterization. However, the reliability of predictions for other loading conditions might heavily depend on the selection of an appropriate material parameter set [37, 38, 39, 40]. While there is a clear *need* for identifying a unique set of parameters, there remains a lack of available research on *how* to accomplish this.

To assess the uniqueness or identifiability of material parameters, optimization algorithms are often initiated at multiple initial values [41, 42]. Alternatively, analyzing the model’s sensitivity to the different parameters can help determine the range of certainty for the best-fit parameters [43, 44]. This approach allows for a systematic analysis of how measurement errors propagate into uncertainty bounds in parameter identification [45].

While it is generally accepted that the uniqueness problem can be tackled by increasing the quantity and richness of experimental data, the sensitivity of the different measurements to changes in the parameters must be examined on a case-by-case basis. Previous studies have investigated various experimental designs and measurement modalities to identify a unique set of material properties through indentation. It has been demonstrated that indentation force–depth data alone cannot yield a unique set of two or more isotropic hyperelastic parameters, and that it is necessary to combine information on shape and force [46, 33, 32, 47]. Uniqueness considerations regarding viscoelastic and poroelastic properties have also been studied [28, 40]. For anisotropic hyperelastic materials, this has been attempted in several ways. One approach involves using an asymmetric indenter while measuring only the indentation force–depth relation [48, 49, 50]. However, this approach requires accurate alignment between the fiber directions and the indenter’s orientation, and misalignment can substantially decrease the certainty in the parameter identification. Another approach involves measuring the contact aspect ratio of the indenter using a stamp indentation, which helps identify the fiber direction, but has limited success at uniquely identifying material properties [51]. Additionally, using different indentation angles has been proposed, though without disclosing any findings regarding the parameter identifiability in this approach [52]. Finally, in-plane deformations of the samples’ bottom surface have been tracked using 2D digital image correlation (DIC) [35, 53]. However, this technique is not applicable *in vivo*, and has demonstrated limited sensitivity of the experimental measurements to changes in certain constitutive parameters.

Considering the high computational demands of iterative iFEA, which involves conducting simulations that closely resemble experimental tests numerous times, it is generally more beneficial to enhance the variety of measurement modalities within a single test rather than to increase the number of tests conducted.

To this end, the current study focuses on identifying hyperelastic transversely isotropic properties through macro-indentation. Our goals are to determine parameter identifiability when utilizing combined measurements of force and surface deformation. We estimate the certainty bounds for each parameter and evaluate the contribution of each measurement to their identification. By examining the quasi-static nonlinear response of a soft composite phantom, we evaluate our results against standardized tests.

## 2. Methods

### 2.1. Overview

The main goal of this research is to investigate the identifiability of homogenized material parameters that characterize anisotropic soft tissues through indentation using iFEA. To evaluate the accuracy of our approach, we employ a synthetic anisotropic composite tissue phantom, for which the material parameters can also be estimated through separate analysis of the composite’s matrix and fiber materials. Given the numerous factors that affect material parameter identification, we perform a numerical sensitivity analysis and carefully consider the certainty in the resulting

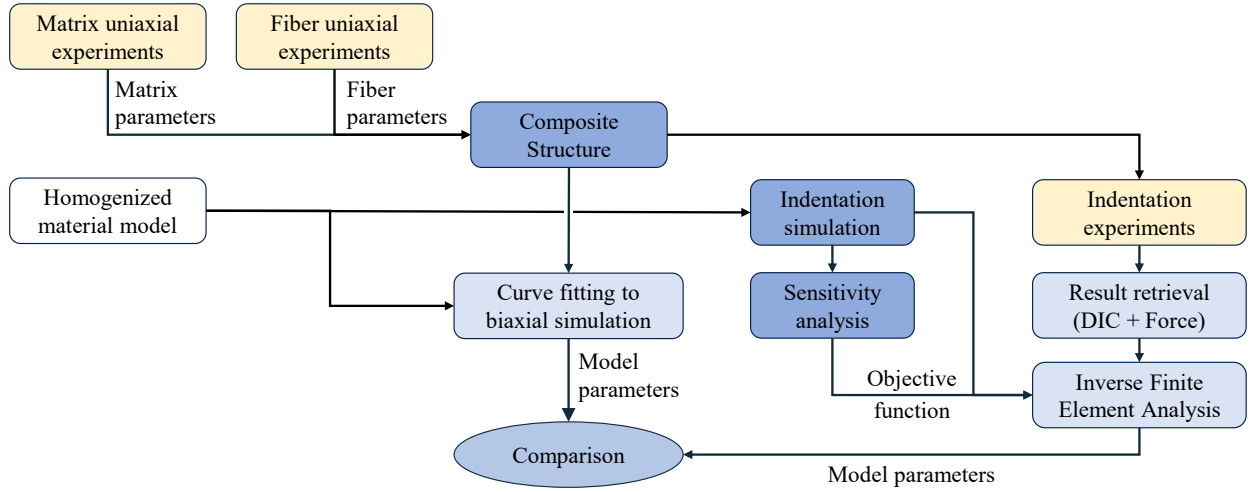


Figure 1: Flowchart of material parameter identification and validation procedures.

material parameter values. To validate our findings, we individually analyze the mechanical properties of the matrix and fiber materials of the composite, which are then used to construct an FEM of the composite and simulate its mechanical response. This response is then fitted to a homogenized anisotropic material model, with the resulting parameters compared to those obtained from performing iFEA of the indentation experiments. The structure of the work is outlined in [Figure 1](#).

## 2.2. Synthetic anisotropic composite phantom preparation

To develop a synthetic anisotropic composite phantom with reproducible properties, we use a platinum-catalyzed silicone-based elastomer as a matrix material to mimic soft tissue-like hyperelastic behavior. While it has been widely used for synthetic tissue phantoms [54, 55, 56], its use in anisotropic tissue phantoms is less explored.

To fabricate the composite specimen, we mold the silicone elastomer into a 3D-printed mold with stiffer fibers. First, we prepare a mold with dimensions of  $100 \times 100 \times 60 \text{ mm}^3$  by sequentially layering 3D-printed sheets of thermoplastic polyurethane (TPU) eTPU-95A (Esun Industrial Co., Ltd., Shenzhen, China), each incorporating 12 uniformly spaced fibers, each having a cross-sectional area of  $1.6 \times 1.6 \text{ mm}^2$ . To ensure alignment and stability, we print the fibers with the surrounding mold material. This process yields an empty shell with evenly distributed fibers. Subsequently, we fill the mold with Ecoflex™ 00-20 silicone (Smooth-On, Inc., Macungie, PA, USA). After curing, we remove the outer TPU shell by cutting the fibers to separate them from the shell. The full process steps and illustrations are detailed in [Appendix A](#). The final composite is a rectangular silicone cuboid encompassing 168 TPU fibers, with a fiber volume fraction (FVF) of 7%. Finally, we apply a thin layer of black silicone paint on the top face and then spray white paint to create a speckle pattern with an approximate feature size of 0.4 mm, as shown in [Figure 2](#).

## 2.3. Composite matrix and fiber material parameter estimation

To establish the "ground truth" material parameters for the composite, we perform uniaxial tests on each individual component material to characterize their mechanical properties. We perform the experiments using an eXpert 8000 planar biaxial system (ADMET, Norwood, MA, USA), equipped with an Interface WMC-50 50 lbf load cell, utilizing only one axis.

To characterize the matrix material, we mold Ecoflex™ 00-20 specimens into cylinders with a radius of 13 mm and a length of 250 mm, and fashion the ends into wedges for secure gripping in the machine. A speckle pattern is applied to the specimen for tracking its deformations with cameras, using DIC. Image processing is carried out using a subset size (SS) of 23 pixels, a step size (ST) of 9 pixels, and a strain window (SW) of 7. The strain tensor is derived from the displacement data using a Green-Lagrange-Q4 polynomial. 30 stretch steps are performed until its length is



Figure 2: TPU-silicone fiber-reinforced transversely isotropic composite. Note the speckle pattern applied to the top surface to allow surface deformation measurement around the indenter, using DIC.

doubled ( $\lambda = 2$ ). The data is extracted quasi-statically, with a pause of at least 30 s between steps. The force and DIC measurements are processed to extract the true stress and the axial and transverse stretches at each deformation step.

Additionally, we perform an unconfined uniaxial compression experiment. We cut the cylinders used in the uniaxial stretch experiments down to a length of 34 mm and place them between two compression plates with a rough contact surface. 15 compression steps are performed at intervals of 0.5 mm until the specimen’s curved surface comes in contact with the plates. The data is extracted quasi-statically, with a pause of at least 30 s between steps. Since this experiment results in non-homogeneous conditions, we identify the material parameters using iFEA. Considering symmetry, we simulate half of the cylinder, apply symmetry boundary conditions, and iterate the FE model parameters to minimize the objective function that describes the discrepancies in force between the measured and simulated values. The final material parameters are the optimized best fit for both tension and compression with equal weights.

For characterizing the fiber material, we conduct uniaxial tension experiments directly on the eTPU-95A filaments. Due to their narrowness, we do not apply DIC and assume incompressibility. The filaments are extended at a rate of 0.01 mm/s until their length is doubled ( $\lambda = 2$ ).

#### 2.4. FE models

All FE simulations are performed using the FE solver FEBio version 4.4 [57]. We use MATLAB 9.13 R2022b (The Mathworks Inc., Natick, MA, USA) with the GIBBON open-source toolbox version 3.5.0 [58] for preprocessing and postprocessing the simulations. All the analyses are performed on a Windows 11 PC equipped with an Intel Core i9-12900K 3.2 GHz CPU and 32GB of RAM.

##### 2.4.1. Homogeneous FE model

The FE model used for the homogeneous constitutive law simulations features a  $50 \times 50 \times 60 \text{ mm}^3$  rectangular cuboid representing a symmetric quarter of the test sample, in order to reduce computation time, and a rigid sphere representing a spherical indenter with radius of  $R = 4.77 \text{ mm}$  as shown in Figure 3, or  $R = 8 \text{ mm}$ . A zero-displacement boundary condition is applied to all bottom nodes. The surface of the spherical rigid indenter is modeled with 320 triangular shell elements (`tri3` in FEBio), and is prescribed with downward vertical displacements to preset indentation depths. Contact was implemented using FEBio’s sliding-elastic contact formulation, with a large coefficient (`fric_coeff = 1 \times 10^8`) to enforce a near-perfect stick condition.

Meshing the specimen with hexahedral elements (`hex8` in FEBio) is generated using Cubit 2023.4 (Coreform LLC, Orem, Utah, USA). A mesh convergence study is performed by comparing the forces and displacements obtained using different mesh densities. Note that although a wide range of material properties is used in the study, it is

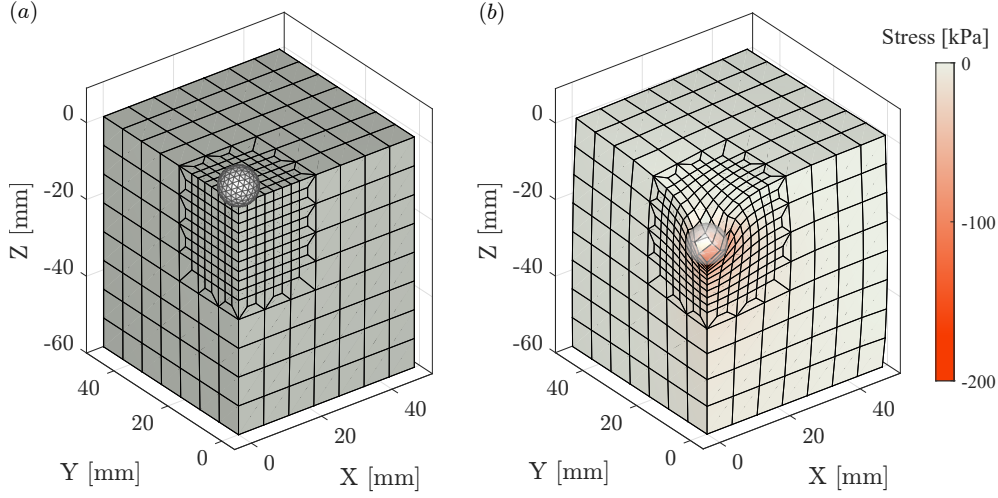


Figure 3: The symmetric quarter homogeneous FE model used in the indentation FEA. (a) View of the nonuniform mesh consisting of linear hexahedral (`hex8`) elements for the specimen, and linear triangular elements (`tri3`) for the rigid indenter. (b) Results of the minimal principal stress values in the last indentation step. Note that the stress is concentrated within the volume with the finer mesh.

assumed that the mesh convergence results obtained using a specific parameter set are applicable to all other sets. We use the constitutive law described in (5b) with the parameters  $c_1 = 9.4$  kPa,  $c_5 = 321$  kPa, and  $\kappa = 1000$  kPa. A very fine mesh (27,255 nodes and 25,841 linear hexahedral elements) serves as the "ground truth" results for evaluating the following mesh convergence errors:

$$\left\{ \begin{array}{l} E_f(N_e) = 100\% \cdot \frac{1}{N_s} \frac{\|\mathbf{F}(N_e) - \mathbf{F}(\tilde{N}_e)\|}{|\mathbf{F}\tilde{N}_e|} \\ E_u(N_e) = 100\% \cdot \frac{1}{N_n(N_e)} \sum_{i=1}^{N_n(N_e)} \frac{\|u^{(i)}(N_e) - u^{(i)}(\tilde{N}_e)\|}{\|u^{(i)}(\tilde{N}_e)\|} \end{array} \right. \quad (1a)$$

$$\left. \begin{array}{l} E_u(N_e) = 100\% \cdot \frac{1}{N_n(N_e)} \sum_{i=1}^{N_n(N_e)} \frac{\|u^{(i)}(N_e) - u^{(i)}(\tilde{N}_e)\|}{\|u^{(i)}(\tilde{N}_e)\|} \end{array} \right\} \quad (1b)$$

where  $N_e$  denotes the number of elements in the mesh,  $\tilde{N}_e$  denotes the number of elements of the "ground truth" mesh,  $N_s$  the number of loading steps, and  $N_n(N_e)$  is the number of surface nodes of the contact surface between the indenter and the cube (DIC measurable displacement).  $\mathbf{F}(N_e)$  denotes the vector of indentation forces at all indentation steps, the vector  $u^{(i)}(N_e)$  denotes the final displacement of the  $i^{th}$  node, and the vector  $u^{(i)}(\tilde{N}_e)$  denotes the "true" final displacement of the  $i^{th}$  node, obtained by interpolating the numerical results of  $\tilde{N}_e$  at the equivalent nodes in the different meshes.

Several different meshes were proposed, differing by the area of refinement and the refinement levels within it. Following the analysis, we choose a model with 1,252 nodes and 1,113 elements that yields a relative error of less than 1%, while maintaining a short runtime of about 6 s, as shown in Figure 4.

#### 2.4.2. Composite model

For validation purposes, we construct an FE model of the TPU-fiber composite. This model features two distinct element sets for the fibers and the matrix, and includes a total of 97,163 nodes and 86,400 `hex8` elements, as shown in Figure 5.

#### 2.5. Constitutive model

To characterize the homogeneous behavior of the composite, we use the transversely isotropic Mooney-Rivlin model (`trans iso Mooney-Rivlin` in FEBio) [59]. The stress-stretch relationship for this model is derived from

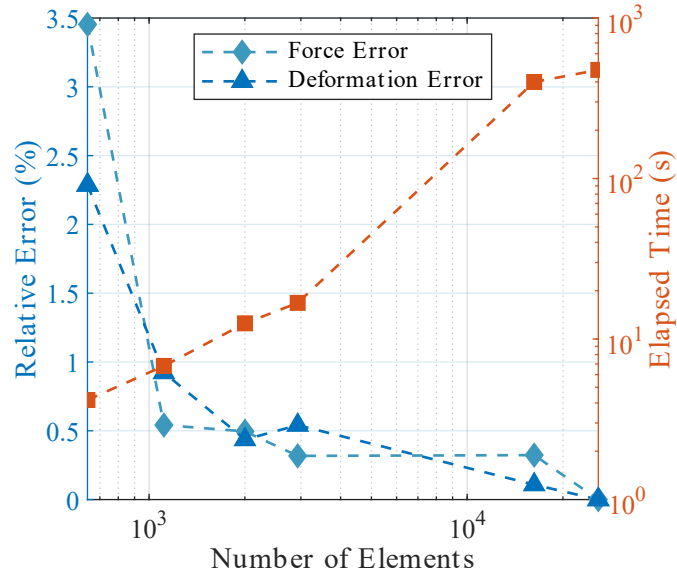


Figure 4: Mesh convergence study results for the homogeneous transversely isotropic hyperelastic FE model under spherical indentation. The relative errors in indentation force and in the deformation of the top surface are presented.

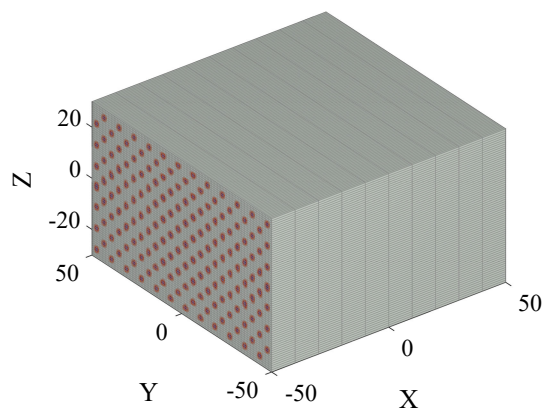


Figure 5: FE model of the anisotropic composite made of TPU fibers in a silicone elastomer matrix.

the following strain energy density (SED) function:

$$\Psi = c_1(I_1 - 3) + c_2(I_2 - 3) + \begin{cases} 0 & \lambda \leq 1 \\ c_3 [e^{-c_4} (\text{Ei}(c_4\lambda) - \text{Ei}(c_4)) - \ln \lambda] & 1 < \lambda < \lambda_m \\ c_5(\lambda - 1) + c_6 \ln \lambda & \lambda \geq \lambda_m \end{cases} \quad (2)$$

where  $I_1$  and  $I_2$  are the first and second invariants of the right Cauchy-Green deformation tensor  $\mathbf{C} = \mathbf{F}^T \mathbf{F}$ ,  $\text{Ei}(\cdot)$  is the exponential integral function,  $\lambda$  is the stretch along the fiber direction ( $\lambda^2 = I_4$ ),  $\boldsymbol{\theta} = \{c_1, c_2, \dots, c_6\}$  are the material parameters, and  $\lambda_m$  is the stretch at which the collagen fibers are straightened. To ensure continuity at  $\lambda = \lambda_m$ , the following condition must be satisfied

$$c_6 = c_3 (e^{c_4(\lambda_m - 1)} - 1) - c_5 \lambda_m \quad (3)$$

This effectively reduces the anisotropy description of the model to a three-parameter formulation [59].

It is important to note that while this incompressible regular form is used for all analytical analyses in this work, we utilize the nearly incompressible equivalent of the constitutive law for numerical computations using FE that uses an uncoupled formulation of the deviatoric and volumetric responses. Consider the deviatoric part of the deformation gradient tensor, defined as  $\tilde{\mathbf{F}} = J^{-1/3} \mathbf{F}$ . Then, the material law can be rewritten as

$$\Psi = c_1(\tilde{I}_1 - 3) + c_2(\tilde{I}_2 - 3) + \frac{1}{2} \kappa (\ln J)^2 + \begin{cases} 0 & \tilde{\lambda} \leq 1 \\ c_3 [e^{-c_4} (\text{Ei}(c_4\tilde{\lambda}) - \text{Ei}(c_4)) - \ln \tilde{\lambda}] & 1 < \tilde{\lambda} < \tilde{\lambda}_m \\ c_5(\tilde{\lambda} - 1) + c_6 \ln \tilde{\lambda} & \tilde{\lambda} \geq \tilde{\lambda}_m \end{cases} \quad (4)$$

where  $\tilde{I}_1$  and  $\tilde{I}_2$  are the first and second invariants of the deviatoric part of the right Cauchy-Green deformation tensor  $\tilde{\mathbf{C}} = \tilde{\mathbf{F}}^T \tilde{\mathbf{F}} = J^{-2/3} \mathbf{C}$ ,  $J \equiv \det(\mathbf{F})$  is the Jacobian of the deformation that quantifies the dilatation, and  $\kappa$  is a bulk modulus-like parameter that penalizes volume changes [60]. By setting  $\kappa = 1000$  kPa, we aim to mitigate potential nonphysical volume changes. This approach ensures that the analytical solutions remain accurate and that the numerical models converge effectively.

Oddes and Solav (2023) [33] deduced that for an isotropic Mooney-Rivlin model, indentation can only be used to identify the sum  $c_1 + c_2$ , which equals half of the initial shear modulus of the material. Given this limitation, we turn to the work of Quapp and Weiss (1998) [61], who demonstrated that for this model setting  $c_2 \neq 0$  only marginally improves the fit to biological materials, aligning with other findings on the insignificance of this parameter [62, 63, 64]. Consequently, we set  $c_2 = 0$ , reducing the isotropic part of the model to a Neo-Hookean form. Further, considering the relation in (3), and since in our test sample the fibers are initially straight ( $\lambda_m = 1$ ), the model is simplified to a fiber-reinforced Neo-Hookean model that is expressed using the following SEDs in the analytical and FE model, respectively:

$$\Psi = c_1(I_1 - 3) + c_5(\sqrt{I_4} - 1) - c_5 \ln \sqrt{I_4} \quad (5a)$$

$$\tilde{\Psi} = c_1(\tilde{I}_1 - 3) + c_5(\sqrt{\tilde{I}_4} - 1) - c_5 \ln \sqrt{\tilde{I}_4} + \frac{\kappa}{2} (\ln J)^2 \quad (5b)$$

## 2.6. Objective function formulation

To determine the  $p$  model parameters  $\boldsymbol{\theta}$  of a constitutive model, we must evaluate  $n > p$  different states of the system. We do this by defining an objective function that quantifies the differences between the simulated model predictions and the experimental results at these states. In this study, the objective function combines four types of relative errors, each reflecting a different aspect of the test sample's behavior under the test conditions: the indentation

force, and the surface displacements in the fiber, transverse, and through-thickness directions ( $\hat{x}$ ,  $\hat{y}$ , and  $\hat{z}$ , respectively). Each value has a corresponding objective function that quantifies the error between the simulation with a trial parameter set  $\theta \in \Theta$  and the experimental or baseline parameter set  $\theta^* \in \Theta$ , where  $\Theta$  is the objective function parameter space.

We define the indentation force error  $F_f$  and in the surface displacements error in the  $j^{\text{th}}$  direction  $F_{u_j}$  as

$$F_f(\theta) = \sum_{\delta=1}^{N_s} \left( \frac{f(\theta; \delta) - f_{exp}(\delta)}{f_{exp}(\delta)} \right)^2 \quad (6a)$$

$$F_{u_j}(\theta) = \sum_{\delta=1}^{N_s} \sum_{i=1}^{N_n} w_j^{(i)} \left( \frac{u_j^{(i)}(\theta; \delta) - u_{j,exp}^{(i)}(\delta)}{\max |u_{j,exp}|} \right)^2 \quad (6b)$$

where  $f(\theta; \delta)$  is the simulated indentation reaction force in the  $\hat{z}$  direction for an indentation depth  $\delta$ ,  $u_j^{(i)}(\theta; \delta)$  and  $u_{j,exp}^{(i)}(\delta)$  are the simulated and experimentally measured displacements of the  $i^{\text{th}}$  node, respectively, with  $j = 1, 2, 3$  indicating the spatial directions  $\hat{x}, \hat{y}, \hat{z}$ , respectively.  $N_n \in \mathbb{N}$  is the number of nodes on the top surface of the mesh, where deformation can be measured using DIC, and  $w_j^{(i)}$  is a weighting factor for the nodal displacements formulated in [Appendix B](#). Lastly,  $N_s$  is the number of loading steps in the experiment and simulation. Note that due to the differing units of displacement fields and force, all terms are normalized to dimensionless quantities. The force balance method [65], defined by (6a), utilizes a normalization term akin to those in previous studies [33, 66, 67]. The local functions (6b) are based on displacement fields, in contrast with most classical approaches that rely on strain fields [68]. Since  $u_{j,exp}$  could be negligibly small at certain points, it may produce a singularity in the objective function. To solve this problem, we use the maximum surface displacement in the experiment as the normalization term. This provides several advantages: it is easy to measure experimentally and compute, it is stable, and it penalizes large deviations more than small ones.

Finally, the four objective functions in (6a) and (6b) are combined into a single objective function using the weighted sum

$$\begin{cases} F(\theta) = \eta_1 F_f + \eta_2 F_{u_1} + \eta_3 F_{u_2} + \eta_4 F_{u_3} \\ \eta_1 + \eta_2 + \eta_3 + \eta_4 = 1, \quad \eta_i \in [0, 1] \end{cases} \quad (7)$$

where  $\eta_i$  are relative weights that are also subject to optimization. For accurate identification of each parameter, the objective function should have sufficient sensitivity in all parameter directions. To that end, we aim to determine the constants  $\eta_i$  that maximize the objective function's sensitivity, or minimize the uncertainty, with respect to each parameter. To achieve this, we quantify the certainty for each parameter using the combined objective function (7) and determine the optimal weights  $\eta_i$  using numerical optimization. The certainty in the identification of each parameter,  $\theta_i$ , is quantified based on the Hessian approximation of the objective function [45]

$$\theta_i = \hat{\theta}_i \pm s \sqrt{2\mathbf{H}_{ii}^{-1}(\hat{\theta})} \quad (\text{no summation on } i) \quad (8)$$

where  $\hat{\theta} \in \Theta$  is the local minima of  $F(\theta)$ ,  $\mathbf{H}$  is the Hessian of the objective function at  $\hat{\theta}$

$$\mathbf{H} = \frac{\partial^2 F}{\partial \theta_j \partial \theta_k} \quad (9)$$

and  $s$  is a statistical estimation of the experimental data

$$s^2 = \left( \frac{p}{n-p} \right) F_{p, n-p}^{1-\alpha} F(\hat{\theta}) \quad (10)$$

where we use a value from the F-distribution, denoted  $F_{p, n-p}^{1-\alpha}$ , with  $p$  and  $n-p$  degrees of freedom, describing the range in which we expect to fall with a confidence level of  $(1-\alpha) \cdot 100\%$  [45].

Initially, we simulate our indentation test using a baseline parameter set  $\hat{\theta} = \theta^*$ , which is a guess presumed to approximate the true material parameters (as further discussed in [subsection 4.2](#)). Then, the optimization algorithm aims to find the constants  $\eta_i$  that minimize the certainty bounds. We use an interior point method optimization via MATLAB's `fmincon` function. This procedure results in the optimal weight configuration for the given experimental setup.

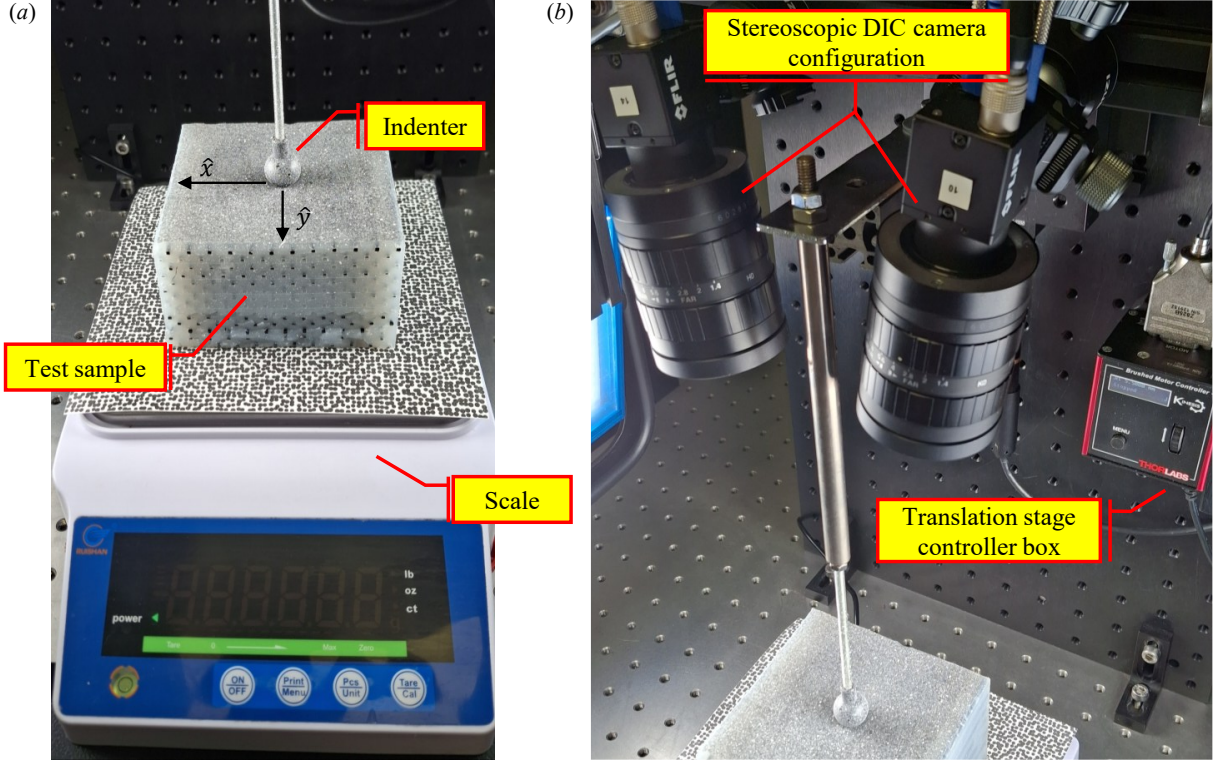


Figure 6: Experimental setup with a sample anisotropic silicone composite. (a) Highlighting the speckle patterns. Note the speckle pattern on the test sample, the indenter, and the scale. (b) The 3D-DIC camera configuration.

### 2.7. Experimental setup

The test setup is shown in Figure 6. The specimen is oriented such that the  $\hat{y}$  is directed towards the fiber direction, and  $\hat{z}$  points upwards towards the indenter. Surface deformations are captured using a stereoscopic 3D-DIC setup, consisting of two Blackfly BFS-U3-51S5M cameras (FLIR LLC, Wilsonville, OR, USA), each equipped with a monochrome Sony IMX264 sensor with a  $2448 \times 2048$  resolution, and a FUJINON HF25SA-1 lens with a focal length of 25 mm. The cameras were arranged in a stereoscopic configuration with a stereo angle of approximately  $20^\circ$ , and a baseline separation of approximately 100 mm. Two spherical indenters, with radii of  $R = 4.77$  mm and  $R = 8.00$  mm, are used for indentation and are connected to a PT1/M-Z8 motorized translation stage (Thorlabs, Inc., Newton, NJ, USA), with a translation accuracy of  $10^{-4}$  mm. Force measurements are continuously captured in 1 s intervals using a RUIZHAN high precision balance scale with a 0.1 g accuracy. A speckle pattern is also applied to the indenter and scale platform to track their spatial positions with respect to the cameras and the specimen. During image processing, a subset size (SS) of 17 pixels, a step size (ST) of 7 pixels, and affine shape functions are employed to calculate displacement data.

A total of 28 indentation steps are performed at 0.5 mm intervals. The data is collected in a quasi-static manner, allowing for a pause of at least 30 s between each indentation step. This pause is used to account for viscoelastic stress relaxation, which causes the force to decay exponentially and approach a constant value after a sufficiently long period [69, 70]. Using MATLAB's `nlinfit` function, we fit the force measurements at each indentation step,  $\delta$ , to an exponential decay function:

$$f_{exp}(\delta, t) = A(\delta)e^{-b(\delta)t} + f_\infty(\delta) \quad (11)$$

where  $A$ ,  $b$ , and  $f_\infty$  are the fitted parameters.  $f_\infty(\delta)$  is the constant value that the force asymptotically approaches as  $t \rightarrow \infty$  for that indentation step, and is taken as the force at static equilibrium.

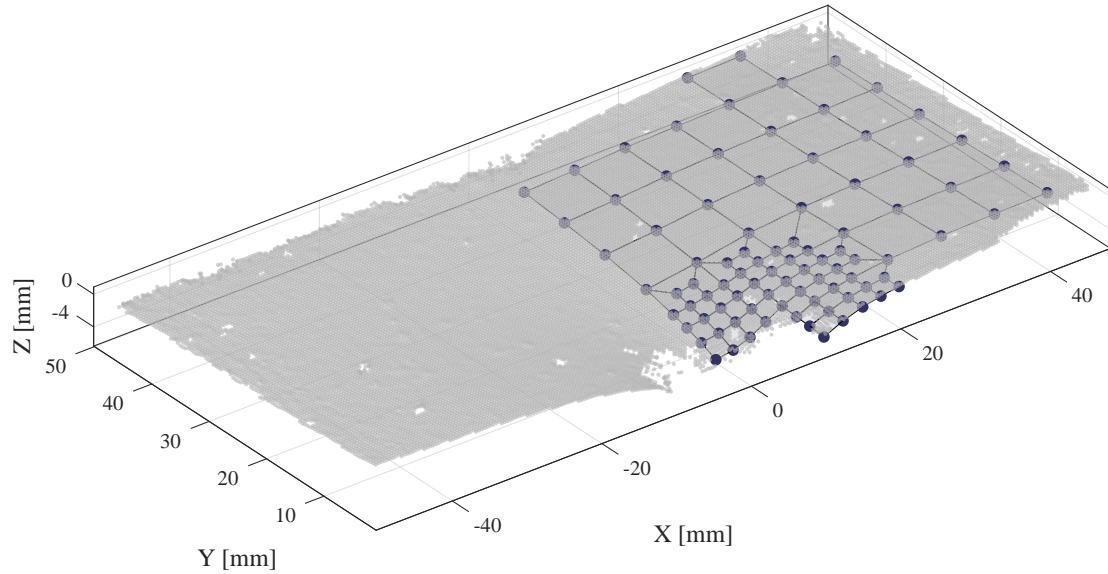


Figure 7: Example of matching between the FE mesh and the DIC data at the maximum indentation depth. Large markers represent the points interpolated at the locations of the FE mesh nodes, and the small gray markers represent the full DIC data.

## 2.8. Analysis of indentation data

### 2.8.1. DIC data processing

To facilitate the comparison between simulated and measured surface displacements, the experimental DIC results are processed to match the FEA nodal positions. This process involves two main steps: spatial registration of the coordinate systems and interpolation of the data points. The 3D displacements are extracted from the stereo images using STEREO 2024.2 DIC software (MatchID, Ghent, Belgium). The data is filtered to exclude regions with poor correlation. Next, the FE mesh and the DIC data are carefully aligned, as even minor misalignments can significantly impact error margins [71]. To align the indenter's position with respect to the specimen, the top surface of the indenter's sphere is also tracked using DIC, and a spherical shape is fitted to these points. The lowest point of the sphere defines the indentation point, which serves as the origin of the coordinate system. The specimen's rotational alignment about the indentation axis is established by aligning the coordinate system's  $\hat{y}$  direction with the fiber direction, which is visible in the DIC images. Once the coordinate systems are matched, the DIC data are interpolated to fit the FE mesh. Interpolating from the finer DIC mesh to the coarser FE mesh can help reduce interpolation errors [65]. To interpolate the data, we use weighted averaging based on proximity, where each FE node on the top surface of the specimen is represented using the positions of its neighboring DIC points in the undeformed reference configurations. Then, the DIC-derived displacement of each FE node at each deformed configuration is computed using a weighted average of the displacements from the neighboring DIC points.

An example of this fitting is shown in Figure 7. Note that some of the surface nodes in the DIC data are obscured during the experiment and are therefore omitted from the fusion process.

Additionally, to examine whether fiber directions can be detected directly from the measured DIC data, we computed the principal directions and values of the strain tensors. This was accomplished using the open-source DIC Matlab toolbox, DuoDIC [72], which utilizes the Cosserat point element method to efficiently compute the deformation tensors of triangular elements in the global 3D coordinate system [73, 74, 75].

### 2.8.2. Inverse finite elements analysis (iFEA)

To perform the iFEA, we compute the objective function that quantifies the error between the simulated and experimentally measured reaction forces and displacement fields, combined using (7). We use MATLAB's optimization routine `lsqnonlin` with the Levenberg–Marquardt algorithm [76], to simultaneously identify the constitutive param-

eters  $c_1$  and  $c_5$  from (5b). The termination criteria are met when the combined objective function value falls below  $3 \times 10^{-2}$ .

### 2.9. Validation

We validate the material parameters derived from indentation experiments by constructing an FE model of the composite, as described in 2.4.2), using the fiber and matrix material parameters obtained as described in 2.3. This model allows two levels of validation: validation of the homogeneous material parameters and validation of the composite FE model itself.

To validate the homogeneous material parameters, we perform an equibiaxial stretch simulation, to which we can analytically fit homogeneous material parameters according to (5a) using

$$\sigma_{11} = 2c_1(\lambda^2 - \lambda^{-4}) + c_5(\lambda - 1) \quad (12a)$$

$$\sigma_{22} = 2c_1(\lambda^2 - \lambda^{-4}) \quad (12b)$$

where  $\lambda$  is the applied stretch, as derived in Appendix C. The stress in the FE model is calculated as the average stress over all elements. We calculate both the longitudinal (in the fiber direction) and the transverse stresses.

To validate the composite FE model itself, we simulate the indentation experiments using the composite FE model (unlike the homogeneous model used in the iFEA), to evaluate the FE simulation's capability to accurately predict the behavior of the physical composite.

## 3. Results

### 3.1. Characterization of component materials

To characterize the mechanical properties of the matrix material (Ecoflex™ 00-20 silicone), we fit the tension and compression data to an incompressible neo-Hookean material model. The fitting results for tension and compression data are shown in Figure 8a and 8c, respectively. Note that since the unconfined compression test results in inhomogeneous deformations, the compressive force-displacement data are used to fit the parameters in an iFEA process, using the FE mesh and setup shown in Figure 8d. This is in contrast to the homogenous uniaxial tension data, which can be expressed as a direct stress-stretch relationship. Furthermore, Figure 8b demonstrates the material's incompressibility, with a Poisson's ratio  $\nu = 0.5$ . This is evident by the relationship between axial stretch  $\lambda_a$  and transverse stretch  $\lambda_t$ , which conforms to the behavior of an ideal incompressible material:  $\lambda_t = \lambda_a^{-1/2}$ .

Fitting of the model to the uniaxial stretch data of the matrix material yields a shear modulus of  $\mu^{(m)} = 13.1 \pm 0.1$  kPa, whereas fitting to the unconfined compression data yields a shear modulus of  $\mu^{(m)} = 31.0 \pm 0.2$  kPa, as depicted in Figure 8a and Figure 8c. The optimized best-fit for the combined tension and compression data results in an intermediate value of  $\mu^{(m)} = 19.4 \pm 0.1$ , as depicted with the light blue line in Figure 8a.

To characterize the mechanical properties of the fiber material (eTPU-95A), we fit the experimental data to a Mooney-Rivlin material model, resulting in the following parameters:  $c_1^{(f)} = -1227 \pm 22$  kPa and  $c_2^{(f)} = 5945 \pm 38$  kPa as shown in Figure 9.

### 3.2. Characterization of the composite

We leverage the components' material parameters found in 3.1, the fiber volume fraction (FVF) of our composite, and the rule of mixtures [77], to estimate an initial guess for the composite's parameters  $c_1$  and  $c_5$ . These parameters form the baseline simulation around which we perform the sensitivity analysis for our iFEA process. While these values provide a useful starting point, they should be regarded as coarse approximations.

$$c_1 = \mu^{(m)}/2 \approx 10 \text{ kPa} \quad (13a)$$

$$c_5 = \text{FVF} \cdot (c_1^{(f)} + c_2^{(f)}) + (1 - \text{FVF}) \cdot c_1 \approx 350 \text{ kPa} \quad (13b)$$

Collectively, we denote these baseline material parameters as

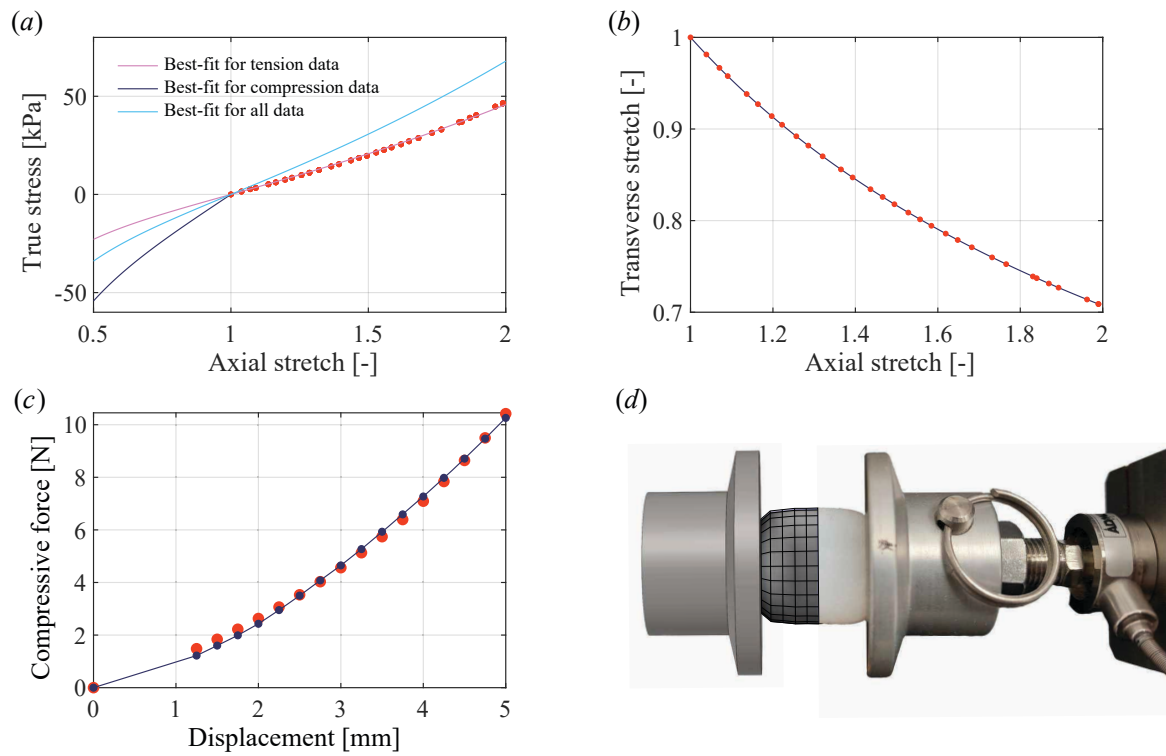


Figure 8: Characterization of Ecoflex™ 00-20 silicone material through uniaxial tension and compression. (a) True stress vs. axial stretch. Red markers denote experimental data from uniaxial tension tests. The purple curve represents the best-fit model to the tension data  $\mu^{(m)} = 13.1$ , the dark blue curve corresponds to an analytical approximation for compression  $\mu^{(m)} = 31.0$  (using the results from (c)), and the light blue curve captures the best-fit model to the combined tension and compression dataset  $\mu^{(m)} = 19.4$ . (b) Transverse and axial stretches for incompressible material and experimental data. Red markers represent the experimental data measured using DIC, and the dark blue curve denotes the theoretical relation for an incompressible material  $\lambda_t = \lambda_a^{-1/2}$ . (c) Measured force vs. compressive displacement. Red markers denote the experimental data from uniaxial compression tests, and dark blue dots denote the best-fit FE simulation results. (d) FE model used in iFEA (left) and physical sample (right) at maximum displacement.

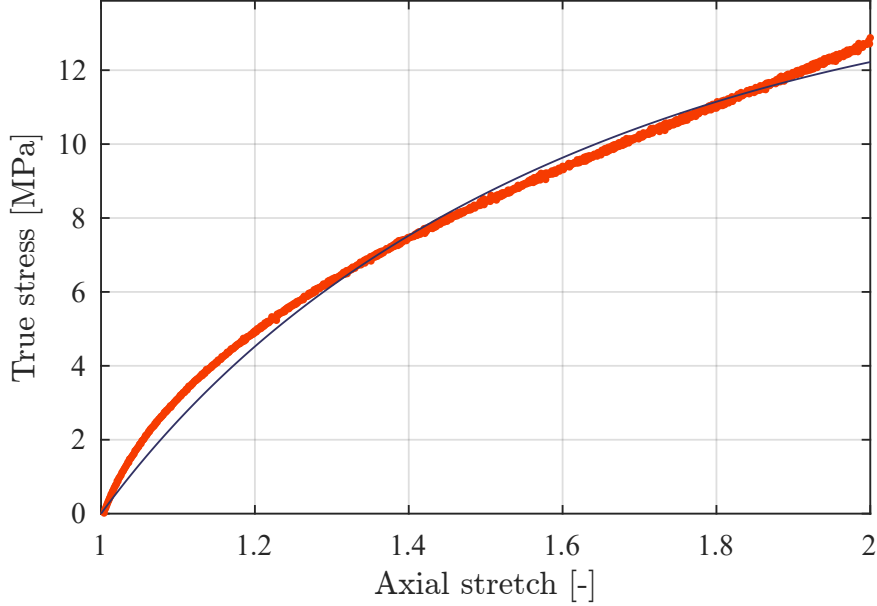


Figure 9: Characterization of eTPU-95A material through axial stretch testing. The plot shows true axial stress vs. axial stretch. Red markers represent experimental data, and the black curve denotes the best-fit ( $R^2 = 0.922$ ) Mooney-Rivlin material model with the fitted parameters:  $c_1^{(f)} = -1227 \pm 22$  kPa and  $c_2^{(f)} = 5945 \pm 38$  kPa.

Table 1: Calculated certainty bounds for  $c_1$  and  $c_5$ , for different objective function compositions using (8) with  $s = 0.05$ . Results are based on the estimates for the fiber-reinforced composite:  $\theta^* = \{c_1, c_5\} = \{10 \text{ kPa}, 350 \text{ kPa}\}$ .

Test design	Parameters		Weights
	$c_1$	$c_5$	$\eta_1, \eta_2, \eta_3, \eta_4$
Only force	$\pm 22.5 \%$	$\pm 210.2 \%$	(1, 0, 0, 0)
Only deformation	$\pm 12.8 \%$	$\pm 50.7 \%$	(0, 0.35, 0.35, 0.3)
Optimal for $c_1$	$\pm 4.5 \%$	$\pm 29.8 \%$	(0.7, 0.3, 0, 0)
Optimal for $c_5$	$\pm 5.4 \%$	$\pm 28.3 \%$	(0.4, 0.35, 0.25, 0)
<b>Combined optimal</b>	<b><math>\pm 5.2 \%</math></b>	<b><math>\pm 28.3 \%</math></b>	<b>(0.45, 0.35, 0.2, 0)</b>

$$\theta^* = \{10 \text{ kPa}, 350 \text{ kPa}\} \quad (14)$$

Next, we run 775 indentation simulations on the homogeneous FE model with combinations of parameters in these ranges  $c_1 \in [1, 21]$  kPa and  $c_5 \in [82.5, 578]$  kPa. We use the procedure described in subsection 2.6 to estimate the optimal objective function weights to obtain the smallest certainty bounds. The results of this step are summarized in Table 1, where we use  $s = 0.05$  for the estimations.

Moving forward, we use the objective function (6) with the combined optimal weights

$$\eta_1 = 0.45, \quad \eta_2 = 0.35, \quad \eta_3 = 0.2, \quad \eta_4 = 0 \quad (15)$$

For these weights, the Hessian at  $\theta^*$  is calculated to be

$$\mathbf{H}(\theta^*) = \begin{bmatrix} 2.07 & -0.12 \\ -0.12 & 0.07 \end{bmatrix} \quad (16)$$

Figure 10 provides a visual representation of the objective function in the normalized parameter space, denoted as  $\bar{\theta} = \{\bar{c}_1, \bar{c}_5\} = c_i/c_i^*$ , such that the baseline parameters are  $\bar{\theta}^* = \{1, 1\}$ . The white ellipse, which is estimated from the Hessian, depicts the region inside which the sets of parameters are practically indistinguishable. Note that although this visualization is only practical for two parameters, the Hessian and the weights estimation method are generalizable to problems with more parameters.

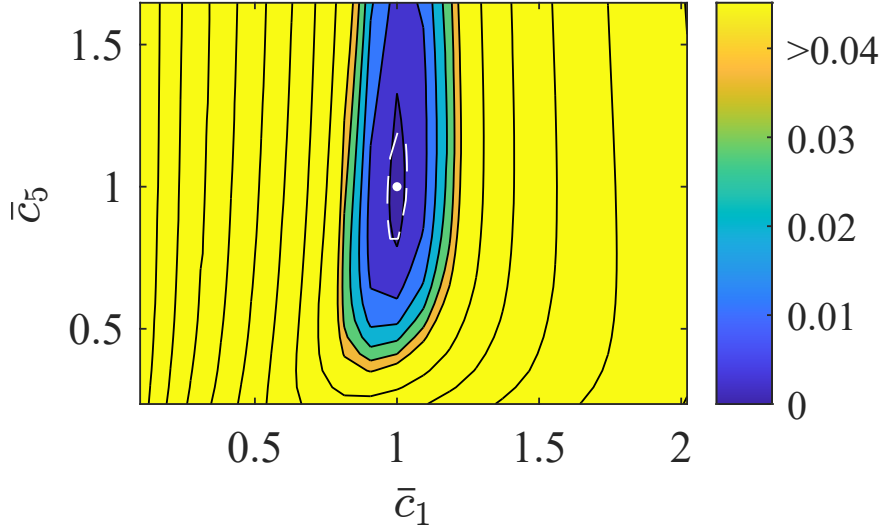


Figure 10: Contour plot depicting the objective function values (6) with weights that maximize the certainty (15). The parameter space is formed of 775 simulations with combinations of parameters in these ranges  $c_1 \in [1, 21]$  kPa and  $c_5 \in [82.5, 578]$  kPa. The white ellipse indicates the isoline representing the estimated certainty region, and the white dot marks the baseline parameters  $\theta^* = \{1, 1\}$ .

### 3.3. Experimental results

The experiment was repeated with two indenter sizes: a small one with a diameter of 9.5 mm, and a large one with a diameter of 16 mm. The experiments included measurements of the reaction force and of the displacements of the top surface, as described in subsection 2.7. The experimental results are illustrated in Figure 11 and Figure 12 for the small and large indenters, respectively. Additionally, Figure 13 plots the measured minimum and maximum principal strains at the last indentation step with the large indenter, as computed using DuoDIC [72].

In both Figure 11 and Figure 12, we note a nonlinear response of the force. The surface deformation results exhibit pronounced anisotropy, as the fiber direction is pulled towards the indenter and the transverse direction bulges outwards. We also note that the fiber direction is clearly visible in the full-field strain results, both in terms of the strain magnitudes and their principal directions, which diverge from perfectly radial and tangential in Figure 13.

### 3.4. Simulation results

#### 3.4.1. Composite indentation simulation

We simulate the experiment as closely as possible using very fine simulations of the composite model, with the material parameters obtained from the uniaxial experiments (subsection 3.1). The indentation-force versus indentation-depth curve, along with the stresses in the deformed configuration at maximum indentation depth, are shown in Figure 14 and Figure 15 for the 9.5 mm indenter and the 16 mm indenter, respectively.

#### 3.4.2. Composite equibiaxial stretch

The equibiaxial stretch simulation on the composite FE model is performed to evaluate the homogenized material parameters analytically, as described in subsection 2.9. Figure 16 presents the simulated true stress versus axial stretch in both the longitudinal (fiber) and transverse directions. Fitting of the homogeneous material model Equation 5 to this data yields the following parameters:  $\theta^* = \{c_1, c_5\} = \{11.61 \pm 0.52 \text{ kPa}, 273 \pm 66 \text{ kPa}\}$ .

### 3.5. Inverse finite element analysis (iFEA)

Using iFEA, we fit the two homogeneous transversely isotropic model parameters to each of the four data sets, as described in subsection 2.8.2. We use the same initial guess of  $\theta_0 = \{c_1, c_5\} = \{6 \text{ kPa}, 300 \text{ kPa}\}$  for all the optimizations. The final fitted parameters are presented in Table 2 alongside their uncertainty bounds, and compared to the parameters fitted using the composite FE simulations. We find that the statistical value of certainty is averaged around  $s = 0.06$ .

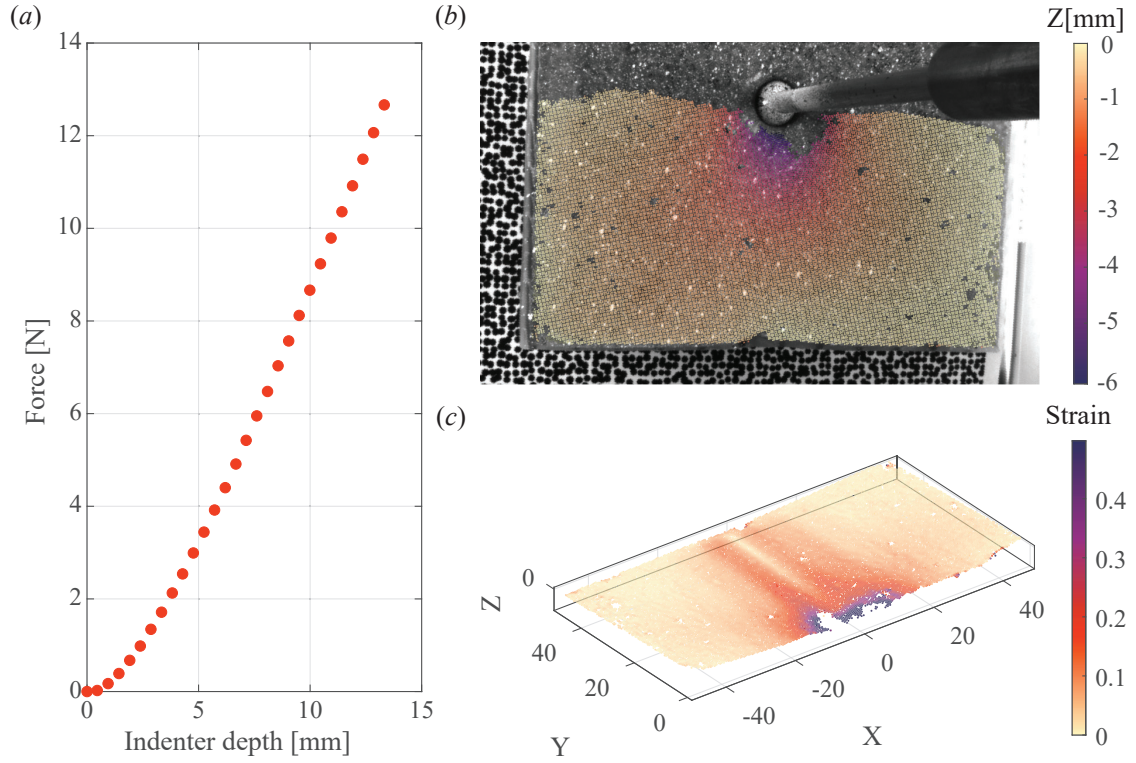


Figure 11: Raw experimental data using a 9.5 mm diameter indenter. (a) Indentation-force versus depth curve, (b, c) depict DIC data scattered in millimeters, at the maximum indentation depth, with (b) showing the displacement in the Z-direction and (c) showing the equivalent Green-Lagrange strain.

Table 2: Final material parameters derived from the iFEA simulations, including calculated certainty bounds for  $c_1$  and  $c_5$  using (8), compared to the simulated biaxial results  $\theta^* = \{c_1, c_5\} = \{11.61 \pm 0.52 \text{ kPa}, 273 \pm 66 \text{ kPa}\}$

Experiment		$c_1$ [kPa]	$c_5$ [kPa]	$F(\hat{\theta})$ [-]
Small Indenter	Experimental	$12.9 \pm 1.1$	$155 \pm 55$	0.015235
	Simulation	$12.42 \pm 0.47$	$92 \pm 16$	0.002656
Large Indenter	Experimental	$11.1 \pm 0.9$	$410 \pm 128$	0.012514
	Simulation	$12.16 \pm 0.63$	$120 \pm 26$	0.005058

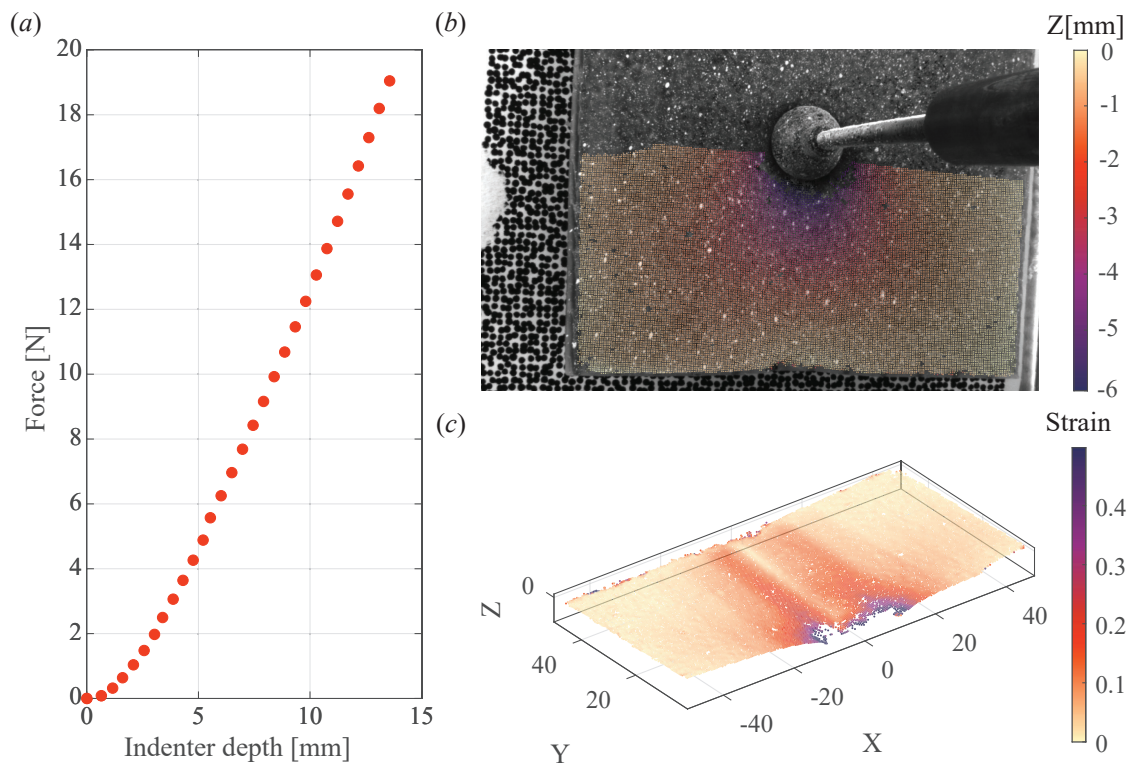


Figure 12: Raw experimental data using a 16 mm diameter indenter. (a) Indentation-force versus depth curve, (b, c) depict DIC data scattered in millimeters, at the maximum indentation depth, with (b) showing the displacement in the Z-direction and (c) showing the equivalent Green-Lagrange strain.

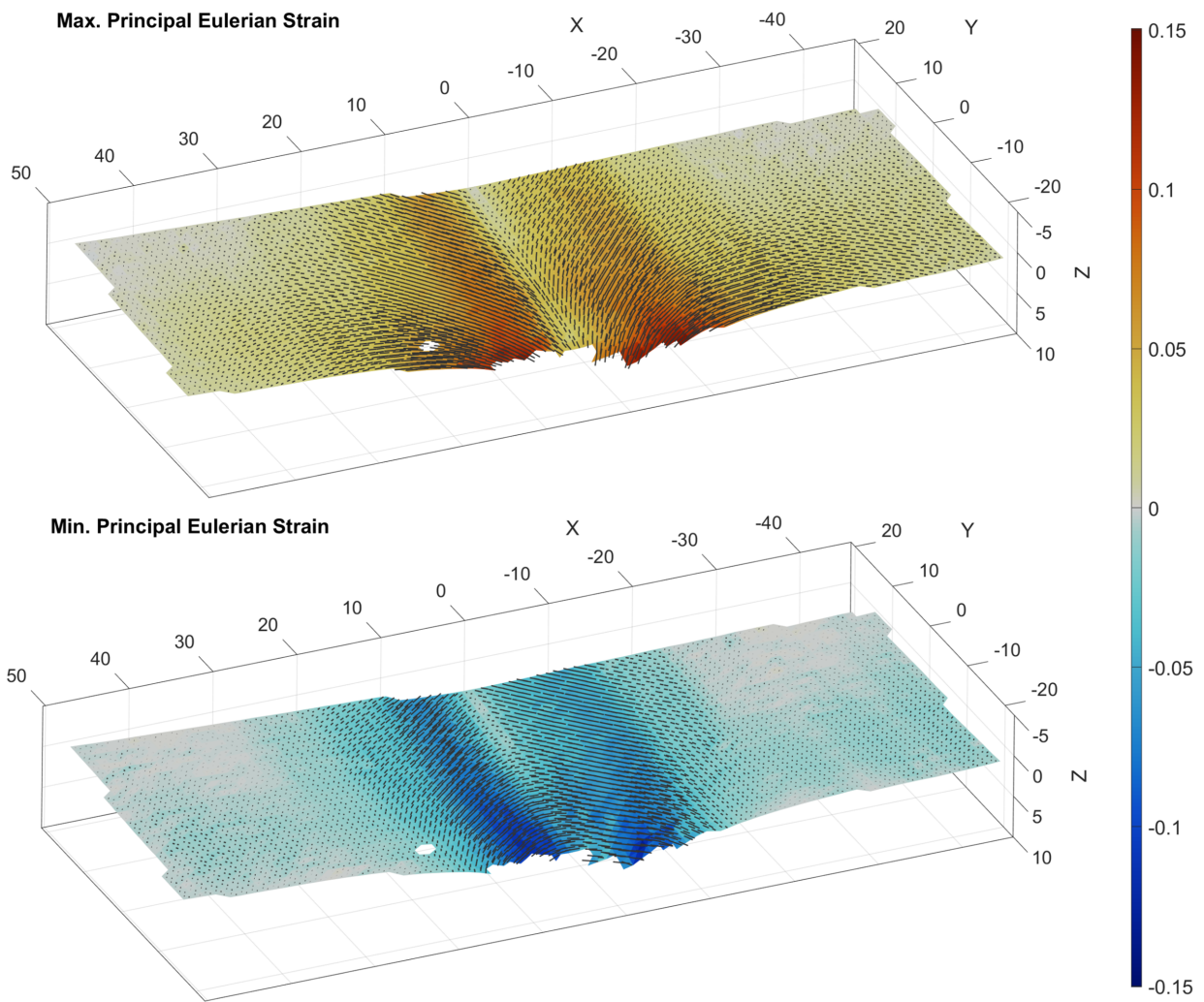


Figure 13: Illustration of the minimal and maximal principal strains computed at the last indentation step using the 16 mm diameter indenter. The colors represent their magnitude, and the black lines represent their directions, with line length proportional to the strain value.

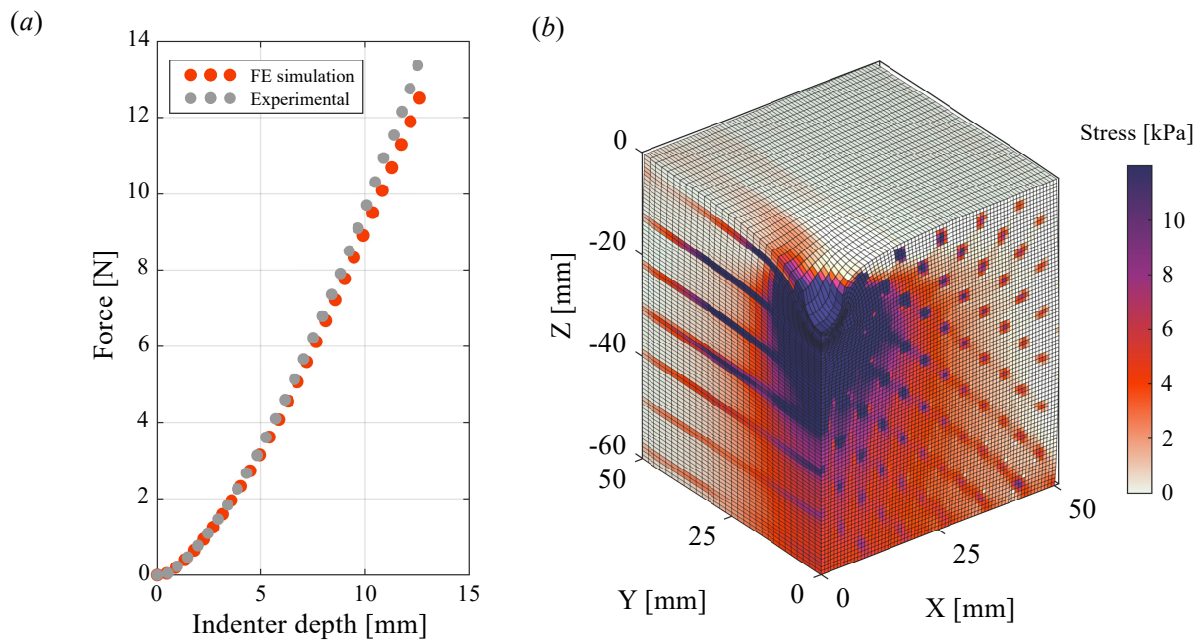


Figure 14: Simulation of the symmetric quarter of a composite FE model using a 9.5 mm diameter indenter. (a) Indentation-force versus indentation-depth curve. Gray circles represent the experimental data, red circles represent the finite-element simulation results. (b) Stress and displacement finite-element simulation results at the maximum indentation depth.

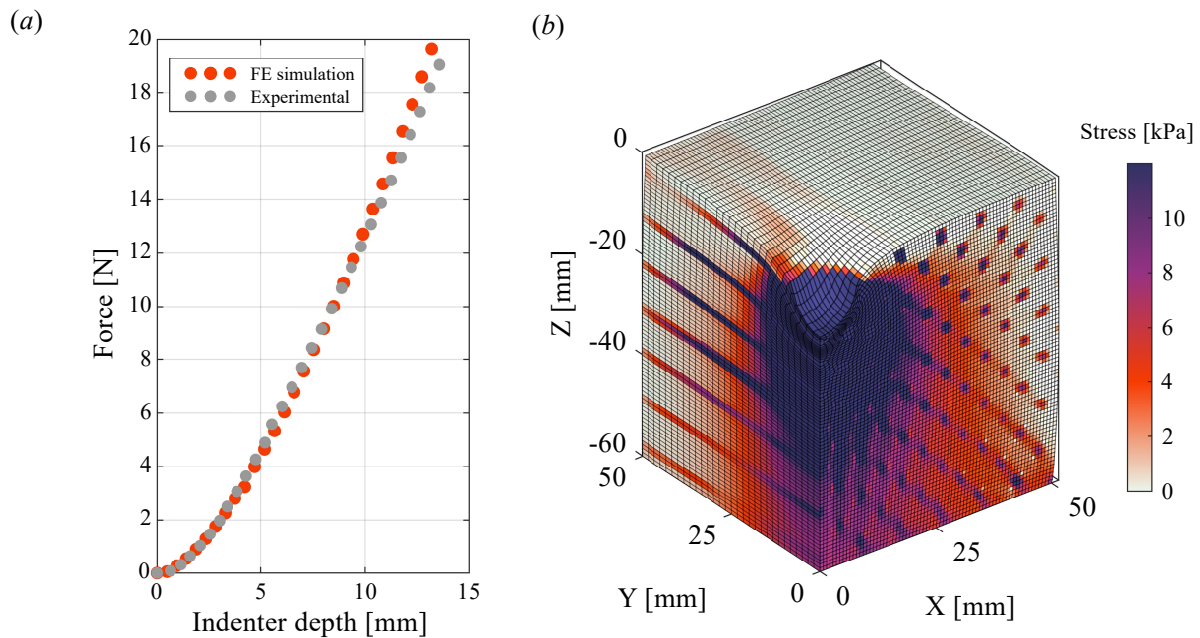


Figure 15: Simulation of the symmetric quarter of a composite FE model using a 16 mm diameter indenter. (a) Indentation-force versus indentation-depth curve. Gray circles represent the experimental data, red circles represent the finite-element simulation results. (b) Stress and displacement finite-element simulation results at the maximum indentation depth.

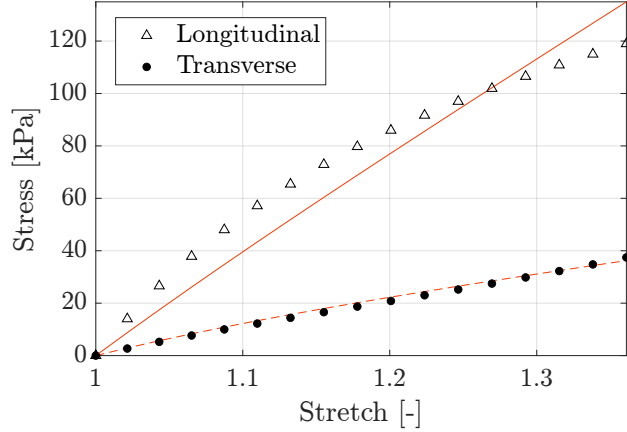


Figure 16: True stress vs axial stretch in both longitudinal (fiber) and transverse directions. Triangles represent calculated stress in the fiber direction, and black dots represent calculated stress in the transverse direction. The red curves represent the theoretical prediction of the homogenized model (5) using (12), where the solid curve is the longitudinal best-fit approximation, and the dashed curve is the transverse best-fit approximation.

## 4. Discussion

This work focuses on the identifiability of the transversely isotropic hyperelastic material parameters from an instrumented indentation test that features full-field surface deformation measurement in addition to indentation force. It has been well established that without careful analysis, the material parameter fitting procedure can result in non-unique solutions, where multiple parameter sets match the experimental data equally well. Additionally, by implementing full-field displacement measurements as an integral part of the indentation test, we reduce the need for conducting multiple separate tests. This approach reduces the computational burden associated with iFEA, allowing a single simulation to yield sufficient data for robust parameter identification.

### 4.1. Effects of measurement modalities on identifiability

By conducting our sensitivity analysis, we determined the relative contribution of each measurement to reducing the certainty range in the identifying each parameter. As shown in Table 1, the smallest uncertainty is obtained using a combination of both force and surface deformation data. This finding supports the inclusion of DIC measurement in the experiment, which is particularly critical for identifying the anisotropic part of the model ( $c_5$  in our case).

We analyzed the experimental data obtained in our experiments using four variables: the indenter’s reaction force and surface displacement in three spatial directions (transverse direction  $\hat{x}$ , fiber direction  $\hat{y}$ , and the direction perpendicular to the top surface  $\hat{z}$ ). The results of the objective function weights, shown in Table 1, reveal that the indentation force data is the most consequential in reducing the uncertainty in the parameters’ estimation. It is highly sensitive to changes in both parameters, especially  $c_1$ . Indeed, typically, identifying material parameters through indentation and iFEA has relied *only* on the indenter’s force-depth data [78, 79]. However, this data alone is insufficient to provide adequate certainty in the parameter estimations, as indicated by the bounds shown in Table 1. Particularly,  $c_5$  practically cannot be estimated as its uncertainty spans  $\pm 210\%$ . In contrast, surface displacement data in the fiber and transverse directions are sensitive to both  $c_1$  and  $c_5$ , enabling the reduction of their uncertainty to  $\pm 5.2\%$  and  $\pm 28\%$ , respectively. This finding highlights the important advantage of using full-field deformation data for material parameter estimation, particularly when anisotropy is considered. Still, despite the rapidly growing use of DIC in uniaxial, biaxial, and inflation tests [80, 81, 82, 83, 84], as well as in vivo [85, 86], its application in indentation remains scarce.

In contrast, the relative difference in the  $\hat{z}$  displacement is of minimal importance. This finding suggests that the material parameters have minimal impact on the  $\hat{z}$  displacements, for an indenter with a specific radius, even for fiber-reinforced anisotropic materials. This observation aligns with the findings of Hertz (1881) [87] and Du et al. (2023) [88], which suggest that the  $\hat{z}$  deformation profile for *isotropic* materials depends solely on the distance from the indenter and its radius, independent of material properties. Moreover, this finding highlights the importance of using a measurement technique that can measure in-plane deformations, as opposed to techniques that only measure shape [89, 21]. Either 3D-DIC or 2D-DIC combined with fringe projection [90] could provide the required data.

#### 4.2. Consistency of the sensitivity analysis

The sensitivity analysis is essential for understanding the model and estimating parameter identifiability before conducting experiments. The results of the sensitivity analysis generally depend on the selection of baseline parameters. Interestingly, in our study, the certainty bounds calculated around the optimized parameters (as detailed in Table 2) differ only marginally from those derived using the initial estimate  $\theta^*$  (see Table 1) and from each another. This indicates that despite potentially significant differences in sensitivity around different baseline parameters (even when using the same model and experimental setup), the certainty estimates derived from both initial and final parameter sets remain relatively consistent, given that these estimates are close. In case the final estimation differs substantially from the initial guess, the sensitivity analysis can be repeated around this set. It is important to note that, in many instances, the material model and the potential range of parameter values are established (e.g., from ex vivo standard tests). Therefore, although the patient- or location-specific parameters are not initially known, establishing a baseline from ex vivo data will be useful in practical scenarios.

Additionally, the optimization process, which determines the optimal weights of the objective function, can be configured to maximize certainty for each parameter individually, rather than relying on a single combined optimal set of weights. This method requires multiple executions of the iFEA pipeline, where each targets a distinct parameter with enhanced certainty bounds. Parameters resolved in prior steps can then be held fixed in subsequent runs.

The values of certainty bounds calculated using (8) depend on the statistically determined variable  $s$  (10). In our sensitivity analysis, a representative estimate of  $s = 0.05$  was adopted prior to experimentation. Although choosing the value of  $s$  might seem critical, the linear dependence of the results on this factor renders its precise value secondary to its relative scaling. A more appropriate approximation of  $s$  can be obtained from prior statistical analysis of the measurement errors [39]. Alternatively,  $s$  can be statistically derived from measurements collected during the experiment, by analyzing the residuals between the experimental data and the model predictions, as well as the amount of data collected [45].

#### 4.3. Parameter identification

The second objective of this work was to identify the material parameters for the anisotropic soft composite material we fabricated. To achieve this, we conducted experiments using two different spherical indenter sizes and performed corresponding FE simulations for each indenter size on the digital composite. Following the procedure suggested by Karduna et al. (1997) [91], we maintain the same indentation depth in both experiments. The larger indenter is intended to deform more fibers, bringing the response of the composite closer to that of the effective homogenized response. Then, by utilizing iFEA, we identified the homogenized material parameters from these two indentation experiments and two FE composite simulations, resulting in four different material parameter sets. The identified parameters are listed in Table 2. The baseline parameters obtained analytically through the biaxial stretch simulation fall within the corresponding certainty regions of the parameters derived from the experiments. However, the parameter  $c_5$  derived from the digital composite exhibits a discrepancy from the baseline parameters.

As predicted by the sensitivity analysis, the parameter  $c_1$  was consistently identified across all four datasets within a 95% confidence interval. Furthermore, the value of  $c_1$  matches closely the baseline value of the biaxial stretch simulation. In contrast, the identification of  $c_5$  is less straightforward, again, as predicted from the sensitivity analysis. Despite the consistent force reactions observed in both the experimental and simulated data, different  $c_5$  values were identified. This discrepancy is attributed to differences in surface displacement.

A possible explanation for the differences in surface deformation between the physical experiment and the composite digital twin simulation lies in our modeling approach for the matrix material. As discussed, this silicone material exhibited a stiffer response to compression than to tension. To better capture its compressive behavior, without complicating the material model, we selected material parameters that compromise its goodness of fit in tension. Although this choice accurately described the force-depth response during indentation, it does not effectively represent the predominantly tensional deformation of the matrix further from the indenter. Consequently, the physical composite's surface deformed more, resulting in increased measured anisotropy compared to its digital twin. Additionally, imperfect adhesion between the fibers and the matrix may further amplify these effects. This discrepancy explains the larger values of  $c_5$  derived from the physical composite's indentation experiments.

#### 4.4. Limitations and future work

This study has several limitations. First, the homogenized constitutive model is quite simplified. Although it captures nonlinear and anisotropic properties, the assumptions made regarding the stretch at which the fibers are straightened ( $\lambda_m = 1$ ) and the consideration of only a single layer of material limit its direct application in vivo. The silicone phantom is designed to fit a simplified two-parameter constitutive law, whereas real anisotropic tissues will typically require additional parameters. Additionally, the tension-compression asymmetry observed in the response of the silicone matrix material was neglected. This simplification can be addressed in future research by incorporating constitutive models that capture this asymmetry (e.g., [92, 93]).

Second, the initial analysis relies on a user-defined range of parameter values, which may not include the true values. If the sensitivity analysis is conducted over an incorrect region of the parameter space, it could affect the accuracy and reliability of the results. This limits the general applicability and requires prior knowledge to make an initial assessment of the model.

Third, the fiber behavior exhibits a level of complexity not fully captured by the current model, resulting in poor identifiability for the parameter  $c_5$ . Even at the model's optimal objective function, certainty remains as low as  $\pm 28\%$ . Addressing this limitation requires more comprehensive experimental data. This can be achieved by incorporating testing the response in multiple directions [52, 94], or utilizing varied indenter geometries [48, 49, 50], while also incorporating full-field displacement measurements. A sensitivity analysis incorporating these variations will allow us to design experiments that more accurately capture the system's full response.

The framework developed here is inherently scalable and can accommodate models with increased parametric complexity, enabling the identification of more physiologically relevant models. Future work could expand the application of this methodology to more complex tissue models, which may include multiple layers, additional anisotropic models [95], pre-tension, viscoelasticity [96], poroelasticity [97], or other time-dependent or multiphase material systems, as well as smaller length scales. Furthermore, this framework can be combined with data-driven or machine learning-based methods for identifying the constitutive laws and their parameters, while also considering the certainty of identification [98, 95, 99, 100].

## 5. Conclusion

This work presents a novel method for identifying material parameters that characterize soft anisotropic tissues through indentation. It addresses a gap in the literature by incorporating full-field surface deformation data as an integral part of the parameter identification process. A notable advantage of this approach lies in having a single experimental configuration with multimodal measurements, which reduces the computational burden associated with iFEA compared to simulating multiple loading scenarios. By combining sensitivity analysis and experimental validation, we determine the identifiability of a two-parameter hyperelastic transversely isotropic model. Our findings demonstrate that integrating surface displacement data substantially reduces the uncertainty in the parameter identification.

As the number of material parameters increases, the problem becomes more complex, increasing the risk of identifiability problems. The methodologies introduced in this work enable researchers to identify such challenges using numerical simulations that can help inform experimental design. The integration of additional measurement modalities can be explored to quantitatively determine how they enhance confidence in the identified parameters. Although the acceptable certainty level is case-dependent, our method provides a straightforward means to quantify this certainty. Ultimately, this can lead to a better understanding of model behavior and improve parameter identification overall.

## Acknowledgements

This study was supported by the Israel Science Foundation grant no. 1750/22 and the Irwin and Joan Jacobs Fellowship. The funders had no role in study design, data collection and analysis, decision to publish, or preparation of the manuscript.

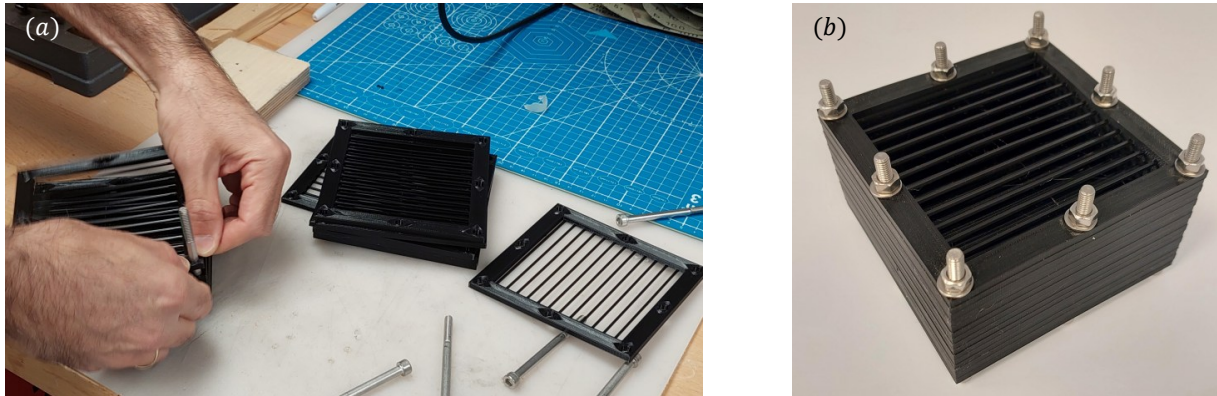


Figure A.17: Mold preparation with 3D-printed TPU sheets and uniformly spaced fibers. (a) Assembling the mold, and (b) the prepared mold.

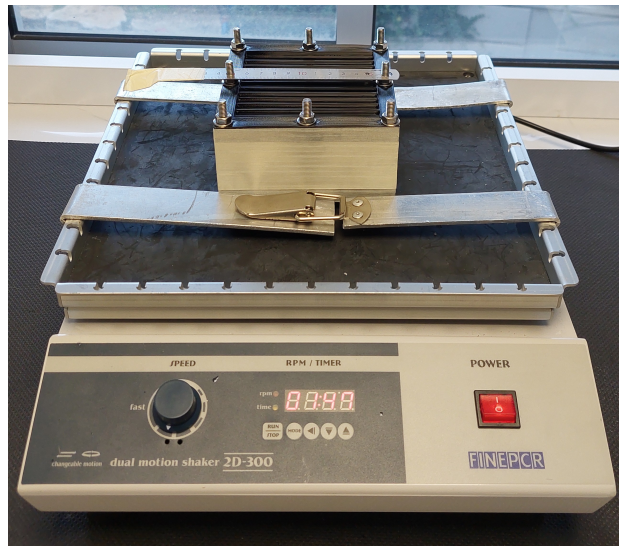


Figure A.18: Vibration plate during subsequent degassing. We use a ruler to hold the mold's shape and prevent the fibers from buckling under the pressure of the bolts. An additional layer of tape is added to keep the tools clean in case of a spill.

## Appendix A. Composite fabrication

To fabricate the composite specimen, we first prepare a mold with dimensions of  $100 \times 100 \times 60 \text{ mm}^3$  by sequentially layering 3D-printed thermoplastic polyurethane (TPU) eTPU-95A sheets as shown in [Figure A.17a](#). Each layer incorporates 12 uniformly spaced fibers and is 4.17 mm high. A bottom plate is added to achieve a total mold height of 60 mm. The fibers have a cross-sectional area of  $1.6 \times 1.6 \text{ mm}^2$ . The layers are secured with bolts to create a tight seal between the layers, as shown in [Figure A.17b](#).

Next, we fill the mold with Ecoflex™ 00-20, prepared by mixing Part A and Part B in a 1:1 ratio. The liquid mixture is degassed in a vacuum chamber to remove any entrapped air, then carefully poured into the mold. To help any remaining trapped bubbles escape the mold, we vibrate the mold on a vibration plate, as shown in [Figure A.18](#). The mold is then allowed to cure overnight at  $25^\circ\text{C}$ . After curing, we remove the outer TPU shell by cutting along the fiber edges to separate them from the outer shell, working layer by layer, as shown in [Figure A.19](#).

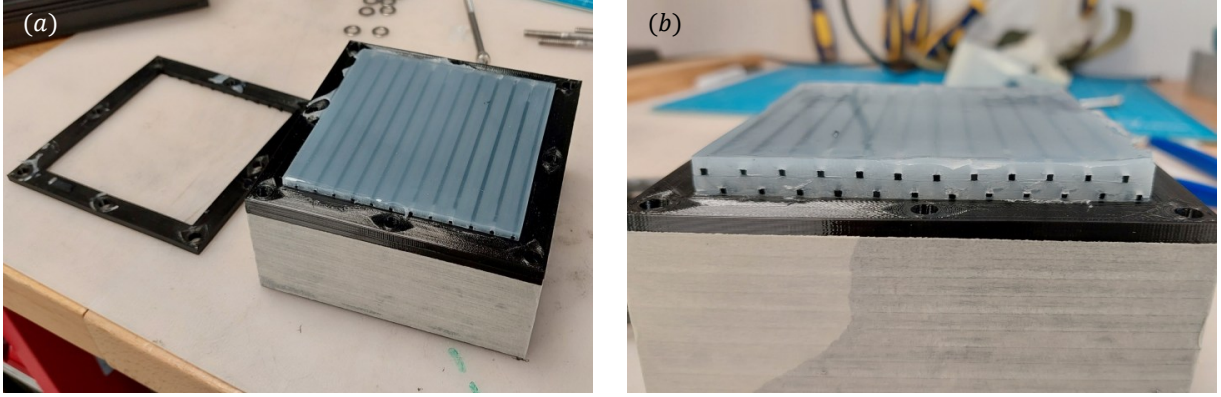


Figure A.19: Removing the outer TPU shell to reveal the composite structure. (a) Process of removing the TPU shell from the mold, while leaving the fibers in the matrix. On the left, a cut TPU sheet is visible. (b) View of fibers in the composite, after being cut from the TPU sheet. Note that the fibers are equally spaced in the composite.

## Appendix B. Nodal weights

The nodal weights used to compute the surface displacement errors in Equation 6b are computed as follows, depending on the node location and the direction of displacement error. Overall, nodal weights are inversely proportional to the distance from the center of the indenter. Additionally, a larger weight is given to the distance from the symmetry line for the weights in the  $\hat{x}$  and  $\hat{y}$  directions. Nodes that have no experimentally obtained deformation data (as detailed in 2.8.1) are assigned a null weight to account for the stereo-camera field of view (FOV) occlusion.

$$\forall i \in [1 : N_{nodes}], \quad w_1^{(i)} = \begin{cases} 0 & \text{if } n_i \text{ is obscured} \\ \frac{(0.1x_i^2 + y_i^2)^{-1/2}}{\sum_{n=1}^N (0.1x_n^2 + y_n^2)^{-1/2}} & \text{else} \end{cases} \quad (\text{B.1})$$

$$\forall i \in [1 : N_{nodes}], \quad w_2^{(i)} = \begin{cases} 0 & \text{if } n_i \text{ is obscured} \\ \frac{(x_i^2 + 0.1y_i^2)^{-1/2}}{\sum_{n=1}^N (x_n^2 + 0.1y_n^2)^{-1/2}} & \text{else} \end{cases} \quad (\text{B.2})$$

$$\forall i \in [1 : N_{nodes}], \quad w_3^{(i)} = \begin{cases} 0 & \text{if } n_i \text{ is obscured} \\ \frac{(x_i^2 + y_i^2)^{-1/2}}{\sum_{n=1}^N (x_n^2 + y_n^2)^{-1/2}} & \text{else} \end{cases} \quad (\text{B.3})$$

(B.1) weights the nodal displacements along  $\hat{x}$  with respect to the distance from the  $x$  symmetry line, (B.2) weighs the nodal displacements along  $\hat{y}$  with respect to the distance from the  $y$  symmetry line, and (B.3) weights the nodal displacements along  $\hat{z}$  with respect to the distance from the indenter.

## Appendix C. Derivation of equibiaxial stress-stretch relations

The Cauchy stress,  $\sigma$  derived from the invariant-based strain energy function  $\Psi$ , can be expressed in terms of the first Piola-Kirchhoff stress tensor  $\mathbf{P} = \partial\Psi/\partial\mathbf{F}$ , to obtain  $\sigma = J^{-1}\mathbf{P}\mathbf{F}^T$  [101]. By considering the incompressible material constitutive law (5), this expression becomes

$$\sigma = J^{-1} \left( \frac{\partial\Psi}{\partial I_1} \frac{\partial I_1}{\partial \mathbf{F}} + \frac{\partial\Psi}{\partial I_4} \frac{\partial I_4}{\partial \mathbf{F}} \right) \mathbf{F}^T - \check{p} \mathbf{I} \quad (\text{C.1})$$

where  $\check{p}$  is the Lagrange multiplier representing the hydrostatic pressure. The derivatives of the invariants are defined as

$$\begin{aligned} \frac{\partial I_1}{\partial \mathbf{F}} &= \frac{\partial I_1}{\partial \mathbf{C}} \frac{\partial \mathbf{C}}{\partial \mathbf{F}} = 2\mathbf{F} \\ \frac{\partial I_4}{\partial \mathbf{F}} &= \frac{\partial I_4}{\partial \mathbf{C}} \frac{\partial \mathbf{C}}{\partial \mathbf{F}} = (\mathbf{a} \otimes \mathbf{a})(2\mathbf{F}) \end{aligned} \quad (\text{C.2})$$

With the assumption of incompressibility  $J = 1$ , we obtain the relation

$$\boldsymbol{\sigma} = \left[ 2c_1 + \left( \frac{c_5}{\sqrt{I_4}} - \frac{c_5}{I_4} \right) \mathbf{a} \otimes \mathbf{a} \right] \mathbf{B} - \check{p} \mathbf{I} \quad (\text{C.3})$$

where  $\mathbf{I}$  is the identity tensor and  $\mathbf{B} = \mathbf{F}\mathbf{F}^T$  is the left Cauchy-Green deformation tensor. For fitting the material parameters  $c_1$  and  $c_5$ , it is convenient to express the constitutive relation in terms of the principal stretches, as described below for the equibiaxial case.

In the equibiaxial extension test, the specimen is equally stretched in two directions with stretch ratios of  $\lambda_1 = \lambda_2 = \lambda$ . With the assumption of incompressibility, the deformation tensor and Cauchy stress tensor can be expressed as

$$\mathbf{F} = \begin{bmatrix} \lambda & 0 & 0 \\ 0 & \lambda & 0 \\ 0 & 0 & \lambda^{-2} \end{bmatrix} \quad (\text{C.4})$$

$$\boldsymbol{\sigma} = \begin{bmatrix} 2c_1\lambda^2 + c_5\lambda - c_5 - \check{p} & 0 & 0 \\ 0 & 2c_1\lambda^2 - \check{p} & 0 \\ 0 & 0 & 2c_1\lambda^{-4} - \check{p} \end{bmatrix} \quad (\text{C.5})$$

As with the uniaxial case,  $\check{p}$  is constant, and the surface in direction  $\mathbf{e}_3$  is free from traction, leading to  $\check{p} = 2c_1\lambda^{-4}$ . Consequently, the stress-stretch relations are

$$\sigma_{11} = 2c_1(\lambda^2 - \lambda^{-4}) + c_5(\lambda - 1) \quad (\text{C.6a})$$

$$\sigma_{22} = 2c_1(\lambda^2 - \lambda^{-4}) \quad (\text{C.6b})$$

Since the fibers are stretched a given amount,  $\sigma_{22}$  is a function only of  $c_1$ , allowing for easier identification.

## References

- [1] S. Fregonese, M. Bacca, Piercing soft solids: A mechanical theory for needle insertion, *Journal of the Mechanics and Physics of Solids* 154 (2021) 104497. URL: <https://www.sciencedirect.com/science/article/pii/S0022509621001654>. doi:10.1016/j.jmps.2021.104497.
- [2] H. Gu, H. Yan, Z. Shi, R. Dan, Finite-element simulation of functional knee sleeves based on three-dimensional modeling of the knee joint, *Textile Research Journal* 95 (2025) 1268–1286. URL: <https://journals.sagepub.com/doi/10.1177/00405175241277020>. doi:10.1177/00405175241277020.
- [3] P. Lu, Z. Liao, Q. Zeng, H. Chen, W. Huang, Z. Liu, Y. Chen, J. Zhong, G. Huang, Customized Three-Dimensional-Printed Orthopedic Close Contact Casts for the Treatment of Stable Ankle Fractures: Finite Element Analysis and a Pilot Study, *ACS Omega* 6 (2021) 3418–3426. URL: <https://pubs.acs.org/doi/10.1021/acsomega.0c06031>. doi:10.1021/acsomega.0c06031.
- [4] E. Vignali, E. Gasparotti, K. Capellini, B. M. Fanni, L. Landini, V. Positano, S. Celi, Modeling biomechanical interaction between soft tissue and soft robotic instruments: importance of constitutive anisotropic hyperelastic formulations, *The International Journal of Robotics Research* 40 (2021) 224–235. URL: <https://journals.sagepub.com/doi/10.1177/0278364920927476>. doi:10.1177/0278364920927476.
- [5] D. R. C. Lee, X. Yang, F. Riccio-Ackerman, B. Alemón, M. Ballesteros-Escamilla, D. Solav, S. R. Lipsitz, K. M. Moerman, C. I. Meyer, A. M. Jaeger, J. C. Huegel, H. M. Herr, A clinical comparison of a digital versus conventional design methodology for transtibial prosthetic interfaces, *Scientific Reports* 14 (2024) 25833. URL: <https://www.nature.com/articles/s41598-024-74504-3>. doi:10.1038/s41598-024-74504-3, publisher: Nature Publishing Group.

- [6] M. Navarro-Lozoya, M. S. Kennedy, D. Dean, J. I. Rodriguez-Devora, Development of phantom material that resembles compression properties of human brain tissue for training models, *Materialia* 8 (2019) 100438. URL: <https://linkinghub.elsevier.com/retrieve/pii/S2589152919302340>. doi:10.1016/j.mtla.2019.100438.
- [7] J. Ock, S. Lee, T. Kim, D. Hong, M. Kim, B. S. Ko, N. Kim, Accuracy evaluation of a 3D printing surgical guide for breast-conserving surgery using a realistic breast phantom, *Computers in Biology and Medicine* 137 (2021) 104784. URL: <https://linkinghub.elsevier.com/retrieve/pii/S0010482521005783>. doi:10.1016/j.combiomed.2021.104784.
- [8] Y. Wang, B. L. Tai, H. Yu, A. J. Shih, Silicone-Based Tissue-Mimicking Phantom for Needle Insertion Simulation, *Journal of Medical Devices* 8 (2014) 021001. URL: <https://asmedigitalcollection.asme.org/medicaldevices/article/doi/10.1115/1.4026508/448103/SiliconeBased-TissueMimicking-Phantom-for-Needle>. doi:10.1115/1.4026508.
- [9] N. Cobetto, C.-E. Aubin, S. Parent, Surgical Planning and Follow-up of Anterior Vertebral Body Growth Modulation in Pediatric Idiopathic Scoliosis Using a Patient-Specific Finite Element Model Integrating Growth Modulation, *Spine Deformity* 6 (2018) 344–350. URL: <https://doi.org/10.1016/j.jspd.2017.11.006>. doi:10.1016/j.jspd.2017.11.006.
- [10] S. P. DiMaio, Modelling, Simulation and Planning of Needle Motion in Soft Tissues, Doctoral thesis, University of British Columbia, Vancouver, Canada, 2003.
- [11] S. Misra, K. T. Ramesh, A. M. Okamura, Modeling of Tool-Tissue Interactions for Computer-Based Surgical Simulation: A Literature Review, *Presence: Teleoperators and Virtual Environments* 17 (2008) 463–491. URL: <https://direct.mit.edu/pvar/article/17/5/463-491/18726>. doi:10.1162/pres.17.5.463.
- [12] I. I. Argatov, X. Jin, L. M. Keer, Collective indentation as a novel strategy for mechanical palpation tomography, *Journal of the Mechanics and Physics of Solids* 143 (2020) 104063. URL: <https://www.sciencedirect.com/science/article/pii/S0022509620302970>. doi:10.1016/j.jmps.2020.104063.
- [13] T. Sun, J. Wang, X. Liu, H. Huang, J. Wang, M. Suo, J. Zhang, Z. Li, Finite element models of intervertebral disc: recent advances and prospects, *Annals of Medicine* 57 (2025) 2453089. URL: <https://www.tandfonline.com/doi/full/10.1080/07853890.2025.2453089>. doi:10.1080/07853890.2025.2453089.
- [14] Y. Zhu, S. Pirola, M. Y. Salmasi, S. Sasidharan, S. M. Fisichella, D. P. O'Regan, J. E. Moore Jr, T. Athanasiou, X. Y. Xu, The Influence of Material Properties and Wall Thickness on Predicted Wall Stress in Ascending Aortic Aneurysms: A Finite Element Study, *Cardiovascular Engineering and Technology* 16 (2025) 52–65. URL: <https://link.springer.com/10.1007/s13239-024-00756-9>. doi:10.1007/s13239-024-00756-9.
- [15] Y. Ishizaki, J. Wang, J. Kim, T. Matsumoto, E. Maeda, Contributions of collagen and elastin to elastic behaviours of tendon fascicle, *Acta Biomaterialia* 176 (2024) 334–343. URL: <https://www.sciencedirect.com/science/article/pii/S174270612400014X>. doi:10.1016/j.actbio.2024.01.014, publisher: Elsevier.
- [16] M. Böl, K. Leichsenring, S. Kohn, Alexander E. Ehret, The anisotropic and region-dependent mechanical response of wrap-around tendons under tensile, compressive and combined multiaxial loads, *Acta Biomaterialia* 183 (2024) 157–172. URL: <https://www.sciencedirect.com/science/article/pii/S1742706124003015>. doi:10.1016/j.actbio.2024.05.053, publisher: Elsevier.
- [17] A. S. Dickinson, J. W. Steer, P. R. Worsley, Finite element analysis of the amputated lower limb: A systematic review and recommendations, *Medical Engineering & Physics* 43 (2017) 1–18. URL: <https://www.sciencedirect.com/science/article/pii/S1350453317300607>. doi:10.1016/j.medengphy.2017.02.008.

- [18] E. Tonuk, M. Silver-Thorn, Nonlinear elastic material property estimation of lower extremity residual limb tissues, *IEEE Transactions on Neural Systems and Rehabilitation Engineering* 11 (2003) 43–53. doi:10.1109/TNSRE.2003.810436, conference Name: IEEE Transactions on Neural Systems and Rehabilitation Engineering.
- [19] E. Bosboom, M. Hesselink, C. Oomens, C. Bouten, M. Drost, F. Baaijens, Passive transverse mechanical properties of skeletal muscle under in vivo compression, *Journal of Biomechanics* 34 (2001) 1365–1368. URL: <https://linkinghub.elsevier.com/retrieve/pii/S0021929001000835>. doi:10.1016/S0021-9290(01)00083-5.
- [20] D. He, D. Malu, Y. Hu, A Comprehensive Review of Indentation of Gels and Soft Biological Materials, *Applied Mechanics Reviews* 76 (2024). URL: <https://doi.org/10.1115/1.4065434>. doi:10.1115/1.4065434.
- [21] R. Remus, C. Sure, S. Selkmann, E. Uttich, B. Bender, Soft tissue material properties based on human abdominal in vivo macro-indenter measurements, *Frontiers in Bioengineering and Biotechnology* 12 (2024). URL: <https://www.frontiersin.org/journals/bioengineering-and-biotechnology/articles/10.3389/fbioe.2024.1384062/full>. doi:10.3389/fbioe.2024.1384062, publisher: Frontiers.
- [22] W. Yuan, Y. Ding, G. Wang, Universal contact stiffness of elastic solids covered with tensed membranes and its application in indentation tests of biological materials, *Acta Biomaterialia* 171 (2023) 202–208. URL: <https://www.sciencedirect.com/science/article/pii/S1742706123005391>. doi:10.1016/j.actbio.2023.09.006.
- [23] M.-G. Zhang, Y.-P. Cao, G.-Y. Li, X.-Q. Feng, Pipette aspiration of hyperelastic compliant materials: Theoretical analysis, simulations and experiments, *Journal of the Mechanics and Physics of Solids* 68 (2014) 179–196. URL: <https://www.sciencedirect.com/science/article/pii/S0022509614000520>. doi:10.1016/j.jmps.2014.03.012.
- [24] S. Diridollou, F. Patat, F. Gens, L. Vaillant, D. Black, J. M. Lagarde, Y. Gall, M. Berson, In vivo model of the mechanical properties of the human skin under suction, *Skin Research and Technology* 6 (2000) 214–221. URL: <https://onlinelibrary.wiley.com/doi/abs/10.1034/j.1600-0846.2000.006004214.x>. doi:10.1034/j.1600-0846.2000.006004214.x, \_eprint: <https://onlinelibrary.wiley.com/doi/pdf/10.1034/j.1600-0846.2000.006004214.x>.
- [25] N. Connesson, N. Briot, P. Y. Rohan, P. A. Barraud, S. A. Elahi, Y. Payan, Bilayer Stiffness Identification of Soft Tissues by Suction, *Experimental Mechanics* 63 (2023) 715–742. URL: <https://link.springer.com/10.1007/s11340-023-00946-x>. doi:10.1007/s11340-023-00946-x.
- [26] A. Erdemir, M. L. Viveiros, J. S. Ulbrecht, P. R. Cavanagh, An inverse finite-element model of heel-pad indentation, *Journal of Biomechanics* 39 (2006) 1279–1286. doi:10.1016/j.jbiomech.2005.03.007.
- [27] S. Avril, S. Evans, *Material Parameter Identification and Inverse Problems in Soft Tissue Biomechanics*, Springer, 2017. URL: <http://link.springer.com/10.1007/978-3-319-45071-1>. doi:10.1007/978-3-319-45071-1, publication Title: Springer International Publishing.
- [28] M. C. Barick, Y. Gaillard, A. Lejeune, F. Amiot, F. Richard, On the uniqueness of intrinsic viscoelastic properties of materials extracted from nanoindentation using FEMU, *International Journal of Solids and Structures* 202 (2020) 929–946. doi:10.1016/J.IJSOLSTR.2020.03.015, publisher: Pergamon.
- [29] R. W. Ogden, G. Saccomandi, I. Sgura, Fitting hyperelastic models to experimental data, *Computational Mechanics* 34 (2004) 484–502. URL: <https://doi.org/10.1007/s00466-004-0593-y>. doi:10.1007/s00466-004-0593-y.
- [30] S. Evans, S. Avril, Identification of material parameters through inverse finite element modelling, *Computer Methods in Biomechanics and Biomedical Engineering* 15 (2012) 1–2. doi:10.1080/10255842.2012.650321.

- [31] T. P. Babarenda Gamage, Constitutive parameter identifiability and the design of experiments for applications in breast biomechanics, Ph.D. thesis, The University of Auckland, 2016.
- [32] N. Fougeron, Z. Oddes, A. Ashkenazi, D. Solav, Identification of constitutive materials of bi-layer soft tissues from multimodal indentations, *Journal of the Mechanical Behavior of Biomedical Materials* 155 (2024) 106572. URL: <https://linkinghub.elsevier.com/retrieve/pii/S1751616124002042>. doi:10.1016/j.jmbbm.2024.106572.
- [33] Z. Oddes, D. Solav, Identifiability of soft tissue constitutive parameters from in-vivo macro-indentation, *Journal of the Mechanical Behavior of Biomedical Materials* 140 (2023) 105708. URL: <https://www.sciencedirect.com/science/article/pii/S1751616123000619>. doi:10.1016/j.jmbbm.2023.105708.
- [34] J. D. Van Tonder, M. P. Venter, G. Venter, A novel method for resolving non-unique solutions observed in fitting parameters to the Mooney Rivlin material model, *Finite Elements in Analysis and Design* 225 (2023) 104006. URL: <https://www.sciencedirect.com/science/article/pii/S0168874X23000999>. doi:10.1016/j.finel.2023.104006, publisher: Elsevier.
- [35] M. A. J. Cox, N. J. B. Driessen, R. A. Boerboom, C. V. C. Bouten, F. P. T. Baaijens, Mechanical characterization of anisotropic planar biological soft tissues using finite indentation: Experimental feasibility, *Journal of Biomechanics* 41 (2008) 422–429. URL: <https://www.sciencedirect.com/science/article/pii/S0021929007003594>. doi:10.1016/j.jbiomech.2007.08.006.
- [36] V. Ayyalasomayajula, O. Ervik, H. Sorger, B. Skallerud, Macro-indentation testing of soft biological materials and assessment of hyper-elastic material models from inverse finite element analysis, *Journal of the Mechanical Behavior of Biomedical Materials* 151 (03-2024) 106389. doi:10.1016/j.jmbbm.2024.106389.
- [37] N. Arnold, J. Scott, T. R. Bush, A review of the characterizations of soft tissues used in human body modeling: Scope, limitations, and the path forward, *Journal of Tissue Viability* 32 (2023) 286–304. URL: <https://www.sciencedirect.com/science/article/pii/S0965206X23000141>. doi:10.1016/j.jtv.2023.02.003.
- [38] R. Keerthiwansa, J. Javorik, J. Kledrowetz, P. Nekoksa, Elastomer testing: the risk of using only uniaxial data for fitting the Mooney-Rivlin hyperelastic-material model, *Materiali in tehnologije* 52 (2018) 3–8. URL: <http://mit.imt.si/Revija/izvodi/mit181/keerthiwansa.pdf>. doi:10.17222/mit.2017.085.
- [39] A. Maček, B. Starman, S. Coppieters, J. Urevc, M. Halilović, Confidence intervals of inversely identified material model parameters: A novel two-stage error propagation model based on stereo DIC system uncertainty, *Optics and Lasers in Engineering* 174 (2024) 107958. URL: <https://www.sciencedirect.com/science/article/pii/S0143816623004876>. doi:10.1016/j.optlaseng.2023.107958.
- [40] J. M. Peloquin, D. M. Elliott, Global and local identifiability analysis of a nonlinear biphasic constitutive model in confined compression, *Journal of The Royal Society Interface* 21 (2024) 20240415. URL: <https://royalsocietypublishing.org/doi/10.1098/rsif.2024.0415>. doi:10.1098/rsif.2024.0415.
- [41] A. Sadeghi Naini, R. V. Patel, A. Samani, Measurement of Lung Hyperelastic Properties Using Inverse Finite Element Approach, *IEEE Transactions on Biomedical Engineering* 58 (2011) 2852–2859. URL: <https://ieeexplore.ieee.org/abstract/document/5936109>. doi:10.1109/TBME.2011.2160637, conference Name: IEEE Transactions on Biomedical Engineering.
- [42] B. N. Safa, M. H. Santare, C. R. Ethier, D. M. Elliott, Identifiability of tissue material parameters from uniaxial tests using multi-start optimization, *Acta Biomaterialia* 123 (2021) 197–207. URL: <https://www.sciencedirect.com/science/article/pii/S1742706121000076>. doi:10.1016/j.actbio.2021.01.006.

- [43] S. Hartmann, R. R. Gilbert, Identifiability of material parameters in solid mechanics, *Archive of Applied Mechanics* 88 (2018) 3–26. URL: <https://doi.org/10.1007/s00419-017-1259-4>. doi:10.1007/s00419-017-1259-4.
- [44] Y. Lanir, O. Lichtenstein, O. Imanuel, Optimal Design of Biaxial Tests for Structural Material Characterization of Flat Tissues, *Journal of Biomechanical Engineering* 118 (1996) 41–47. URL: <https://doi.org/10.1115/1.2795944>. doi:10.1115/1.2795944.
- [45] A. Ashkenazi, D. Solav, Parameter certainty quantification in nonlinear models, *International Journal of Engineering Science* 206 (2025) 104163. URL: <https://www.sciencedirect.com/science/article/pii/S0020722524001472>. doi:10.1016/j.ijengsci.2024.104163.
- [46] Y. Pan, Y. Zhan, H. Ji, X. Niu, Z. Zhong, Can hyperelastic material parameters be uniquely determined from indentation experiments?, *RSC Advances* 6 (2016) 81958–81964. URL: <https://xlink.rsc.org/?DOI=C6RA15747E>. doi:10.1039/C6RA15747E.
- [47] J. D. Van Tonder, M. P. Venter, G. Venter, A New Method for Improving Inverse Finite Element Method Material Characterization for the Mooney–Rivlin Material Model through Constrained Optimization, *Mathematical and Computational Applications* 28 (2023) 78. URL: <https://www.mdpi.com/2297-8747/28/4/78>. doi:10.3390/mca28040078.
- [48] J. E. Bischoff, Static Indentation of Anisotropic Biomaterials Using Axially Asymmetric Indenters—a Computational Study, *Journal of Biomechanical Engineering* 126 (2004) 498–505. URL: <https://doi.org/10.1115/1.1785808>. doi:10.1115/1.1785808.
- [49] Y. Feng, R. J. Okamoto, R. Namani, G. M. Genin, P. V. Bayly, Measurements of mechanical anisotropy in brain tissue and implications for transversely isotropic material models of white matter, *Journal of the Mechanical Behavior of Biomedical Materials* 23 (2013) 117–132. URL: <https://www.sciencedirect.com/science/article/pii/S175161611300129X>. doi:10.1016/j.jmbbm.2013.04.007.
- [50] R. Namani, Y. Feng, R. J. Okamoto, N. Jesuraj, S. E. Sakiyama-Elbert, G. M. Genin, P. V. Bayly, Elastic Characterization of Transversely Isotropic Soft Materials by Dynamic Shear and Asymmetric Indentation, *Journal of Biomechanical Engineering* 134 (2012) 061004. URL: <https://asmedigitalcollection.asme.org/biomechanical/article/doi/10.1115/1.4006848/427258/Elastic-Characterization-of-Transversely-Isotropic>. doi:10.1115/1.4006848.
- [51] A. O. Moghaddam, J. Wei, J. Kim, A. C. Dunn, A. J. Wagoner Johnson, An indentation-based approach to determine the elastic constants of soft anisotropic tissues, *Journal of the Mechanical Behavior of Biomedical Materials* 103 (2020) 103539. URL: <https://linkinghub.elsevier.com/retrieve/pii/S1751616119308306>. doi:10.1016/j.jmbbm.2019.103539.
- [52] A. O. Moghaddam, M. R. Arshee, Z. Lin, M. Sivaguru, H. Phillips, B. L. McFarlin, A. J. W. Johnson, Orientation-dependent indentation reveals the crosslink-mediated deformation mechanisms of collagen fibrils, *Acta Biomaterialia* 158 (2023) 347–357. doi:<https://doi.org/10.1016/j.actbio.2023.01.005>.
- [53] S. Fang, J. McLean, L. Shi, J.-S. Y. Vink, C. P. Hendon, K. M. Myers, Anisotropic Mechanical Properties of the Human Uterus Measured by Spherical Indentation, *Annals of Biomedical Engineering* 49 (2021) 1923–1942. URL: <https://doi.org/10.1007/s10439-021-02769-0>. doi:10.1007/s10439-021-02769-0.
- [54] J. L. Sparks, N. A. Vavalle, K. E. Kasting, B. Long, M. L. Tanaka, P. A. Sanger, K. Schnell, T. A. Conner-Kerr, Use of Silicone Materials to Simulate Tissue Biomechanics as Related to Deep Tissue Injury, *Advances in Skin & Wound Care* 28 (2015) 59–68. URL: <https://journals.lww.com/00129334-201502000-00004>. doi:10.1097/01.ASW.0000460127.47415.6e.

- [55] L. Bernardi, R. Hopf, A. Ferrari, A. E. Ehret, E. Mazza, On the large strain deformation behavior of silicone-based elastomers for biomedical applications, *Polymer Testing* 58 (2017) 189–198. URL: <https://www.sciencedirect.com/science/article/pii/S0142941816312089>. doi:10.1016/j.polymertesting.2016.12.029.
- [56] G. Hattab, T. Ahlfeld, A. Klimova, A. Koepp, M. Schuerer, S. Speidel, Uniaxial compression testing and Cauchy stress modeling to design anatomical silicone replicas, *Scientific Reports* 10 (2020) 11849. URL: <https://www.nature.com/articles/s41598-020-68886-3>. doi:10.1038/s41598-020-68886-3, publisher: Nature Publishing Group.
- [57] S. A. Maas, B. J. Ellis, G. A. Ateshian, J. A. Weiss, FEBio: Finite Elements for Biomechanics, *Journal of Biomechanical Engineering* 134 (2012) 11005–NaN. URL: <https://www.ncbi.nlm.nih.gov/pmc/articles/PMC3705975/>. doi:10.1115/1.4005694.
- [58] K. M Moerman, GIBBON: The Geometry and Image-Based Bioengineering add-On, *The Journal of Open Source Software* 3 (2018) 506. URL: <http://joss.theoj.org/papers/10.21105/joss.00506>. doi:10.21105/joss.00506.
- [59] M. A. Puso, J. A. Weiss, Finite element implementation of anisotropic quasi-linear viscoelasticity using a discrete spectrum approximation, *Journal of Biomechanical Engineering* 120 (1998) 62–70. doi:10.1115/1.2834308.
- [60] J. C. Simo, R. L. Taylor, Quasi-incompressible finite elasticity in principal stretches. continuum basis and numerical algorithms, *Computer Methods in Applied Mechanics and Engineering* 85 (1991) 273–310. doi:10.1016/0045-7825(91)90100-K.
- [61] K. M. Quapp, J. A. Weiss, Material Characterization of Human Medial Collateral Ligament, *Journal of Biomechanical Engineering* 120 (1998) 757–763. URL: <https://asmedigitalcollection.asme.org/biomechanical/article/120/6/757/398068/Material-Characterization-of-Human-Medial>. doi:10.1115/1.2834890.
- [62] M. A. Moreno-Mateos, S. Wiesheier, A. Esmacili, M. Hossain, P. Steinmann, Biaxial characterization of soft elastomers: experiments and data-adaptive configurational forces for fracture, 2025. URL: <http://arxiv.org/abs/2505.20244>. doi:10.48550/arXiv.2505.20244, arXiv:2505.20244 [cond-mat].
- [63] M. Sasso, G. Palmieri, G. Chiappini, D. Amodio, Characterization of hyperelastic rubber-like materials by biaxial and uniaxial stretching tests based on optical methods, *Polymer Testing* 27 (2008) 995–1004. URL: <http://dx.doi.org/10.1016/j.polymertesting.2008.09.001>. doi:10.1016/j.polymertesting.2008.09.001, publisher: Elsevier Ltd.
- [64] M.-G. Zhang, Y.-P. Cao, G.-Y. Li, X.-Q. Feng, Spherical indentation method for determining the constitutive parameters of hyperelastic soft materials, *Biomechanics and Modeling in Mechanobiology* 13 (2014) 1–11. URL: <http://link.springer.com/10.1007/s10237-013-0481-4>. doi:10.1007/s10237-013-0481-4.
- [65] B. Chen, B. Starman, M. Halilović, L. A. Berglund, S. Coppieters, Finite Element Model Updating for Material Model Calibration: A Review and Guide to Practice, *Archives of Computational Methods in Engineering* (2024). URL: <https://link.springer.com/10.1007/s11831-024-10200-9>. doi:10.1007/s11831-024-10200-9.
- [66] P. Liseicka-Graca, J. Majta, K. Muszka, Full-Field Strain Measurement and Numerical Analysis of a Microalloyed Steel Subjected to Deformation with Strain Path Change, *Materials* 13 (2020) 5543. URL: <https://www.mdpi.com/1996-1944/13/23/5543>. doi:10.3390/ma13235543, number: 23 Publisher: Multidisciplinary Digital Publishing Institute.

- [67] R. Gras, H. Leclerc, F. Hild, S. Roux, J. Schneider, Identification of a set of macroscopic elastic parameters in a 3D woven composite: Uncertainty analysis and regularization, *International Journal of Solids and Structures* 55 (2013) 2–16. URL: <https://www.sciencedirect.com/science/article/pii/S0020768313004964>. doi:10.1016/j.ijsolstr.2013.12.023.
- [68] S. Avril, M. Bonnet, A.-S. Bretelle, M. Grédiac, F. Hild, P. Ienny, F. Latourte, D. Lemosse, S. Pagano, E. Pagnacco, F. Pierron, Overview of Identification Methods of Mechanical Parameters Based on Full-field Measurements, *Experimental Mechanics* 48 (2008) 381–402. URL: <https://doi.org/10.1007/s11340-008-9148-y>. doi:10.1007/s11340-008-9148-y.
- [69] M. H. Esteki, A. A. Alemrajabi, C. M. Hall, G. K. Sheridan, M. Azadi, E. Moeendarbary, A new framework for characterization of poroelastic materials using indentation, *Acta Biomaterialia* 102 (2020) 138–148. URL: <https://linkinghub.elsevier.com/retrieve/pii/S1742706119307500>. doi:10.1016/j.actbio.2019.11.010.
- [70] P. M. A. Mitalski, THE MODELING OF FINITE STRAIN VISCOELASTIC MATERIALS, Ph.D. thesis, Purdue University, 2022.
- [71] P. Lava, E. M. C. Jones, L. Wittevrongel, F. Pierron, Validation of finite-element models using full-field experimental data: Levelling finite-element analysis data through a digital image correlation engine, *Strain* 56 (2020) e12350. URL: <https://onlinelibrary.wiley.com/doi/abs/10.1111/str.12350>. doi:10.1111/str.12350, eprint: <https://onlinelibrary.wiley.com/doi/pdf/10.1111/str.12350>.
- [72] D. Solav, A. Silverstein, DuoDIC: 3D Digital Image Correlation in MATLAB, *Journal of Open Source Software* 7 (2022) 4279. URL: <https://joss.theoj.org/papers/10.21105/joss.04279>. doi:10.21105/joss.04279.
- [73] D. Solav, M. B. Rubin, A. Wolf, Soft Tissue Artifact compensation using Triangular Cosserat Point Elements (TCPEs), *International Journal of Engineering Science* 85 (2014) 1–9. URL: <http://dx.doi.org/10.1016/j.ijengsci.2014.07.001>. doi:10.1016/j.ijengsci.2014.07.001, publisher: Elsevier Ltd.
- [74] D. Solav, V. Camomilla, A. Cereatti, A. Barré, K. Aminian, A. Wolf, Bone orientation and position estimation errors using Cosserat point elements and least squares methods: Application to gait, *Journal of Biomechanics* 62 (2017) 110–116. URL: <http://linkinghub.elsevier.com/retrieve/pii/S0021929017300398>. doi:10.1016/j.jbiomech.2017.01.026.
- [75] D. Solav, H. Meric, M. B. Rubin, D. Pradon, F. Lofaso, A. Wolf, Chest Wall Kinematics Using Triangular Cosserat Point Elements in Healthy and Neuromuscular Subjects, *Annals of Biomedical Engineering* 45 (2017) 1963–1973. URL: <http://www.ncbi.nlm.nih.gov/pubmed/28451990>. doi:10.1007/s10439-017-1840-6, ISBN: 1043901718406.
- [76] D. W. Marquardt, An Algorithm for Least-Squares Estimation of Nonlinear Parameters, *Journal of the Society for Industrial and Applied Mathematics* 11 (1963) 431–441. URL: <https://www.jstor.org/stable/2098941>, publisher: Society for Industrial and Applied Mathematics.
- [77] M. W. Tham, M. N. Fazita, H. Abdul Khalil, N. Z. Mahmud Zuhudi, M. Jaafar, S. Rizal, M. M. Haafiz, Tensile properties prediction of natural fibre composites using rule of mixtures: A review, *Journal of Reinforced Plastics and Composites* 38 (2019) 211–248. URL: <https://doi.org/10.1177/0731684418813650>. doi:10.1177/0731684418813650, publisher: SAGE Publications Ltd STM.
- [78] H. Liu, K. Sangpradit, M. Li, P. Dasgupta, K. Althoefer, L. D. Seneviratne, Inverse finite-element modeling for tissue parameter identification using a rolling indentation probe, *Medical & Biological Engineering & Computing* 52 (2014) 17–28. URL: <https://doi.org/10.1007/s11517-013-1118-6>. doi:10.1007/s11517-013-1118-6.

- [79] B. Pierrat, D. B. MacManus, J. G. Murphy, M. D. Gilchrist, Indentation of heterogeneous soft tissue: Local constitutive parameter mapping using an inverse method and an automated rig, *Journal of the Mechanical Behavior of Biomedical Materials* 78 (2018) 515–528. URL: <https://www.sciencedirect.com/science/article/pii/S1751616117301534>. doi:10.1016/j.jmbbm.2017.03.033.
- [80] K. F. Mallett, E. M. Arruda, Digital image correlation-aided mechanical characterization of the antero-medial and posterolateral bundles of the anterior cruciate ligament, *Acta Biomaterialia* 56 (2017) 44–57. URL: <http://dx.doi.org/10.1016/j.actbio.2017.03.045>. doi:10.1016/j.actbio.2017.03.045, publisher: Acta Materialia Inc.
- [81] R. Readioff, B. Geraghty, E. Comerford, A. Elsheikh, A full-field 3D digital image correlation and modelling technique to characterise anterior cruciate ligament mechanics ex vivo, *Acta Biomaterialia* 113 (2020) 417–428. URL: <https://doi.org/10.1016/j.actbio.2020.07.003>. doi:10.1016/j.actbio.2020.07.003, publisher: Elsevier Ltd.
- [82] M. Alloisio, T. C. Gasser, Fracture of porcine aorta—Part 2: FEM modelling and inverse parameter identification, *Acta Biomaterialia* 167 (2023) 158–170. URL: <https://www.sciencedirect.com/science/article/pii/S1742706123003458>. doi:10.1016/j.actbio.2023.06.020.
- [83] K. M. Myers, B. Coudrillier, B. L. Boyce, T. D. Nguyen, The inflation response of the posterior bovine sclera, *Acta Biomaterialia* 6 (2010) 4327–4335. URL: <https://www.sciencedirect.com/science/article/pii/S1742706110002734>. doi:10.1016/j.actbio.2010.06.007.
- [84] P.-Y. Lee, G. Fryc, J. Gnalian, B. Wang, Y. Hua, S. Waxman, F. Zhong, B. Yang, I. A. Sigal, Direct measurements of collagen fiber recruitment in the posterior pole of the eye, *Acta Biomaterialia* 173 (2024) 135–147. URL: <https://www.sciencedirect.com/science/article/pii/S1742706123006608>. doi:10.1016/j.actbio.2023.11.013.
- [85] D. Solav, K. M. Moerman, A. M. Jaeger, H. M. Herr, A Framework for Measuring the Time-Varying Shape and Full-Field Deformation of Residual Limbs Using 3-D Digital Image Correlation, *IEEE Transactions on Biomedical Engineering* 66 (2019) 2740–2752. URL: <https://ieeexplore.ieee.org/document/8625546/>. doi:10.1109/tbme.2019.2895283.
- [86] M. Hokka, N. Mirow, H. Nagel, M. Irsusi, S. Vogt, V.-T. Kuokkala, In-vivo deformation measurements of the human heart by 3D Digital Image Correlation, *Journal of Biomechanics* 48 (2015) 2217–2220. URL: <https://www.sciencedirect.com/science/article/pii/S0021929015001852?via%3Dihub>. doi:10.1016/J.JBIOMECH.2015.03.015, publisher: Elsevier.
- [87] H. Hertz, The Contact of Elastic Solids, *J Reine Angew, Math* 92 (1881) 156–171. URL: <https://cir.nii.ac.jp/crid/1572824500725939840>.
- [88] Y. Du, P. Stewart, N. A. Hill, H. Yin, R. Penta, J. Köry, X. Luo, R. Ogden, Nonlinear indentation of second-order hyperelastic materials, *Journal of the Mechanics and Physics of Solids* 171 (2023) 105139. URL: <https://linkinghub.elsevier.com/retrieve/pii/S0022509622003155>. doi:10.1016/j.jmps.2022.105139.
- [89] Y. Yang, K.-L. Yung, T. W. R. Hung, K.-M. Yu, Analyzing Liver Surface Indentation for In Vivo Refinement of Tumor Location in Minimally Invasive Surgery, *Annals of Biomedical Engineering* 49 (2021) 1402–1415. URL: <https://www.ncbi.nlm.nih.gov/pmc/articles/PMC8058013/>. doi:10.1007/s10439-020-02698-4.
- [90] K. Genovese, A. Montes, A. Martínez, S. L. Evans, Full-surface deformation measurement of anisotropic tissues under indentation, *Medical Engineering and Physics* 37 (2015) 484–493. doi:10.1016/j.medengphy.2015.03.005, iISBN: 1873-4030 (Electronic)\r1350-4533 (Linking).

- [91] A. R. Karduna, H. R. Halperin, F. C. P. Yin, Experimental and numerical analyses of indentation in finite-sized isotropic and anisotropic rubber-like materials, *Annals of Biomedical Engineering* 25 (1997) 1009–1016. URL: <https://doi.org/10.1007/BF02684136>. doi:10.1007/BF02684136.
- [92] Z. Du, G. Zhang, T. Guo, S. Tang, X. Guo, Tension-compression asymmetry at finite strains: A theoretical model and exact solutions, *Journal of the Mechanics and Physics of Solids* 143 (2020) 104084. URL: <https://www.sciencedirect.com/science/article/pii/S0022509620303185>. doi:10.1016/j.jmps.2020.104084.
- [93] K. M. Moerman, C. K. Simms, T. Nagel, Control of tension-compression asymmetry in Ogden hyperelasticity with application to soft tissue modelling, *Journal of the Mechanical Behavior of Biomedical Materials* 56 (2016) 218–228. doi:10.1016/j.jmbbm.2015.11.027.
- [94] S. L. Evans, C. A. Holt, Measuring the mechanical properties of human skin *in vivo* using digital image correlation and finite element modelling, *The Journal of Strain Analysis for Engineering Design* 44 (2009) 337–345. URL: <http://journals.sagepub.com/doi/10.1243/03093247JSA488>. doi:10.1243/03093247JSA488, ISBN: 0309-3247/r2041-3130.
- [95] O. Z. Tikenoğulları, A. K. Açıkan, E. Kuhl, H. Dal, Data-driven hyperelasticity, Part II: A canonical framework for anisotropic soft biological tissues, *Journal of the Mechanics and Physics of Solids* 181 (2023) 105453. URL: <https://www.sciencedirect.com/science/article/pii/S0022509623002570>. doi:10.1016/j.jmps.2023.105453.
- [96] D. Garcia-Gonzalez, A. Jérusalem, S. Garzon-Hernandez, R. Zaera, A. Arias, A continuum mechanics constitutive framework for transverse isotropic soft tissues, *Journal of the Mechanics and Physics of Solids* 112 (2018) 209–224. URL: <https://www.sciencedirect.com/science/article/pii/S0022509617304921>. doi:10.1016/j.jmps.2017.12.001.
- [97] M. Wang, S. Liu, Z. Xu, K. Qu, M. Li, X. Chen, Q. Xue, G. M. Genin, T. J. Lu, F. Xu, Characterizing poroelasticity of biological tissues by spherical indentation: An improved theory for large relaxation, *Journal of the Mechanics and Physics of Solids* 138 (2020) 103920. URL: <https://www.sciencedirect.com/science/article/pii/S0022509620301563>. doi:10.1016/j.jmps.2020.103920.
- [98] Q. Jiao, Y. Chen, J.-h. Kim, C.-F. Han, C.-H. Chang, J. J. Vlassak, A machine learning perspective on the inverse indentation problem: uniqueness, surrogate modeling, and learning elasto-plastic properties from pile-up, *Journal of the Mechanics and Physics of Solids* 185 (2024) 105557. URL: <https://www.sciencedirect.com/science/article/pii/S0022509624000231>. doi:10.1016/j.jmps.2024.105557.
- [99] D. K. Klein, M. Fernández, R. J. Martin, P. Neff, O. Weeger, Polyconvex anisotropic hyperelasticity with neural networks, *Journal of the Mechanics and Physics of Solids* 159 (2022) 104703. URL: <https://linkinghub.elsevier.com/retrieve/pii/S0022509621003215>. doi:10.1016/j.jmps.2021.104703.
- [100] X. Hong, P. Wang, W. Yang, J. Zhang, Y. Chen, Y. Li, A multiscale Bayesian method to quantify uncertainties in constitutive and microstructural parameters of 3D-printed composites, *Journal of the Mechanics and Physics of Solids* 193 (2024) 105881. URL: <https://www.sciencedirect.com/science/article/pii/S0022509624003478>. doi:10.1016/j.jmps.2024.105881.
- [101] J. Bonet, R. D. Wood, *Nonlinear Continuum Mechanics for Finite Element Analysis*, 2nd ed., Cambridge University Press, NY, USA, 2008.